Design of A Modular soft Robotic Arm with Proprioceptive Capabilities



Wenye Ouyang

Mansfield College

University of Oxford

A thesis submitted for the degree of

MSc by Research in Engineering Science

Trinity 2022

Abstract

Proprioception is a trending topic in the field of soft robotics. It endows soft robots with the capability to retrieve their spatial configurations without external feedback for closed-loop control. This is usually achieved by embedding soft and stretchable sensors in the soft bodies of the robot to directly measure their deformations. In addition, taking advantage of their infinite DoFs and inherent compliance, multisegment soft robotic arms are designed to execute highly dexterous tasks in the cluttered environment. However, the integration of the proprioceptive sensors in the body of the soft arm is an ongoing challenge.

Firstly, the embedded sensors need to accommodate for the compliance of the soft robotic arm. Secondly, where to place such sensors is a non-trivial problem. Lastly, the integration of these stretchable sensors involves complex fabrication steps.

In this thesis, we aimed to address these challenges of proprioceptive soft robotic arm with our highly integrated solution - a multisegment soft robotic arm that is capable of proprioceptive sensing while minimising the number of sensors on-board. The proprioceptive sensors do not interfere with the motion of our soft robotic arm and they can be easily integrated and removed. The major contribution of our work is an novel sensing method for modular soft robotic arms. We also advanced this field by contributing: 1) an omnidirectional actuator design for multi-material 3D printing, 2) a modular approach for fast arm assembling and maintenance. By placing sensing arrays within the rigid joints, the variations of stress distribution over the top of segments were measured. Together with the shape information captured by the motion capture system, we obtained a dataset to train a mapping from the tactile sensor responses to the posture of the soft robotic arm using k-nearest neighbors regression. The experimental results demonstrated that the proposed approach was able to reconstruct the whole 3D shape of a three-segment soft robotic arm under piecewise constant curvature assumption.

Acknowledgements

First and foremost, I would like to thank Perla, my dearest supervisor. I remember back in 2019 when we did not have access to the lab and had to do silicone casting in her office which eventually became an extension to our lab. Perla has always been supportive, even during the toughest times of the pandemic. It is a true pleasure to have her as a supervisor and I appreciate what she has done for me and the lab.

Secondly, I would like to thank the Postdocs for their help and valuable discussions - You have taught me how to become a scientist more than just an engineer. Additionally, I thank my colleagues for their companionship, and wish them the best for their research and future endeavors.

Lastly, as well as their financial support, my parents, Hualing and Yongjun, have been loving me unconditionally. Their encouragement to explore the world has always motivated me, and I will continue to do so.

Contents

1 Introduction **1**
1.1 Challenges . . . 2
1.2 Contributions . . . 3

2 Literature review **7**
2.1 Challenges in proprioceptive soft robotic arm . . . 7
2.2 Progress in proprioceptive soft robotic arm . . . 8

3 Motivation and Methodology **17**
3.1 Modular soft robotic arm design . . . 17
3.2 Soft robotic arm proprioception . . . 19

4 Modular soft robotic arm **21**
4.1 Module design . . . 21
4.2 Experimental setup . . . 26
4.3 Experimental characterisation . . . 28

5 Proprioception of soft robotic arm using in-joint sensors **33**
5.1 Stress distribution and soft robot motion . . . 33
5.2 Piecewise constant curvature kinematic model . . . 37
5.3 k-NN regressor . . . 38
5.4 Experimental validation . . . 41

6 Conclusions **45**
6.1 Limitations . . . 46

References **47**

1 Introduction

Soft robotics has become an emerging research area, opening up new possibilities and applications by creating resilient, adaptive, and safe robots which take advantage of their inherent compliance [Rus and Tolley [2015]] to address engineering challenges that traditional robots with rigid links and joints are not suitable for [Schmitt et al. [2018]]. In contrast with rigid robots that have been widely used in the manufacturing industry, soft robots are naturally safer to coexist with human users and to navigate through cluttered environment as they are lightweight and made up of compliant materials which minimise the risks of the hazards that may occur during the physical interactions. With the inherent safety rooted in the materials, Rossiter and Hauser [2016] suggested that we will witness more and wider applications in factories, private spaces and public spaces. There have been notable attempts to apply the soft robotics technology to solve real-world engineering challenges [El-Atab et al. [2020]]. Among all the different applications of soft robotics technology, soft robotic arms have attracted the interest of many researchers. By nature of their inherent compliance, they exhibit infinite number of degrees of freedom (DoF). With these properties, they are expected to be deployed in confined environments to execute highly dexterous tasks autonomously [Marchese et al. [2014]; Satheeshbabu et al. [2020]]. However, their deformable and compliant nature renders the closed-loop control for soft robotic arm challenging. Recent research works have investigated several control strategies relying on external cameras or stretchable sensors such as capacitive sensors, piezoresistive sensors and optical sensors to retrieve the spatial configurations of their robots [Wang et al. [2018c]].

Relying on motion capture systems to provide visual feedback of the posture, several control methods have been proposed to realise feedback posture control of their multisegment soft robotic arms [Katzschmann et al. [2019a,b]; Della Santina et al. [2020a]; Satheeshbabu et al. [2020]]. However, this solution is unfeasible in environments where the visual feedback is impaired by obstacles and environmental lighting.

Alternatively, a more robust solution is to introduce proprioception to the soft robotic arm to retrieve or predict its spatial configuration [Wang et al. [2018c]]. One intuitive method is to embed flexible and stretchable strain sensors such as piezoresistive sensors, capacitive sensors

and optical sensors in the soft robots [Lucarotti et al. [2015]; Van Meerbeek et al. [2018]; Xie et al. [2020]]. These sensors deform with the soft bodies to measure the local deformations of the robots. Using this method, Soter et al. [2018]; Toshimitsu et al. [2021]; Truby et al. [2020] achieved the reconstruction of the complete spatial configuration of their soft robotic arms but the integration of the sensors was complicated and it was impossible to repair and replace the sensors as they were embedded across the bodies.

Luo et al. [2017] and Ozel et al. [2015] retrieved the bending angle of their bidirectional bending soft actuators using hall effect sensors. As the embedded magnets move with respect to the sensors, the variations in the magnetic field are measured to estimate the deformations of the actuator. However, the rigidity of magnets hinders the integration and the performances are naturally influenced by the environmental magnetic field variations [Wang et al. [2018c]].

To reduce the number of on-board proprioceptive sensors and mitigate the undesired variations in the mechanical properties of the sensorised soft robot caused by sensor integration, Scimeca et al. [2019] presented a solution which employs a single piece of sensing array placed on the top of a soft continuum robot. They have demonstrated that the posture of a tendon-driven soft robot can be correlated to the stress distribution over its top captured by the sensor. However, this method has only been validated on a single-segment continuum body.

1.1 Challenges

With the existing approaches that embed proprioceptive sensors across the soft body of the robot, the integration of proprioceptive sensors is a non-trivial process which poses challenges to both design and manufacturing. The integration of stretchable and soft sensors requires multiple fabrication steps which can be complicated and time-consuming [Tapia et al. [2020]]. Moreover, the embedded sensors can impair the inherent compliance of the soft robots and therefore affect the robot's behaviours. Besides, since the proprioceptive sensors stretch and deform with the soft robot, noise signals or even sensing failures can be caused by sliding and detachment between the sensor and the robot [He et al. [2018]].

The workspace of a soft robotic arm is determined by its length. Merely extending the soft arm leads to difficulty in the control due to high response time and gravity effects in the system [Katzschmann et al. [2019b]], and makes it difficult to provide accurate proprioceptive feedback. Similar to rigid robotic arms, one solution is to adopt a modular design that allows the designers to focus on the control and sensorisation of individual segments [Phillips et al. [2018]; Katzschmann et al. [2019a]]. However, the existing modular designs of multisegment

soft robotic arms do not allow access to the proprioceptive sensors after the integration steps which renders repairing the sensing system impossible. In addition, according to [Terryn et al. [2021]], soft robots are susceptible to various types of damage but it is impossible to replace the broken modules with the current modular designs.

It is worth mentioning that the length of the soft module is limited by the capability of the actuation system, the material properties, and the dimensions of the embedded sensors. A single module is not able to bend beyond about 40 degrees if it is short because of the stiffness of the material. If the module is too long, the sensors might not be responsive to the local deformations as they are placed on the top of the module.

In addition, the traditional casting technique usually demands fine moulds and multi-steps processes to fabricate soft robots and the complexity increases when it comes to manufacturing internal volumes [Katzschmann et al. [2019a]]. As a solution to this, multi-material 3D printing techniques are employed to offer more freedom to fabricate complex 3D geometries [Schmitt et al. [2018]].

1.2 Contributions

In this project, we aim to fulfill the following objectives to tackle the challenges described in the previous section to realise proprioceptive sensing for soft robotic arms:

1. To avoid interference with the compliance of the soft robot;
2. To reduce the steps of the integration of the soft robotic arm and the proprioceptive sensors;
3. To ensure the durability of the system by allowing maintenance and replacement of the sensor and the individual module.

An overview of the proprioceptive soft robotic arm system is provided in Fig. 1.1. We modified a design of an omnidirectional bending actuator presented in [He et al. [2021]] that is specifically designed with a bellow structure and constraint beams to be suitable for multi-material 3D printing. Then we fabricated it directly with a multi-material 3D printer. Furthermore, we added joint connectors to the end-plates of the robot so multiple robots could be interconnected to form a multisegment soft robotic arm and each segment could be easily integrated or removed after fabrication.

In order to retrieve the spatial configuration of the soft robotic arm without visual feedback, we extended the approach presented in [Scimeca et al. [2019]] from an one-segment tendon-driven

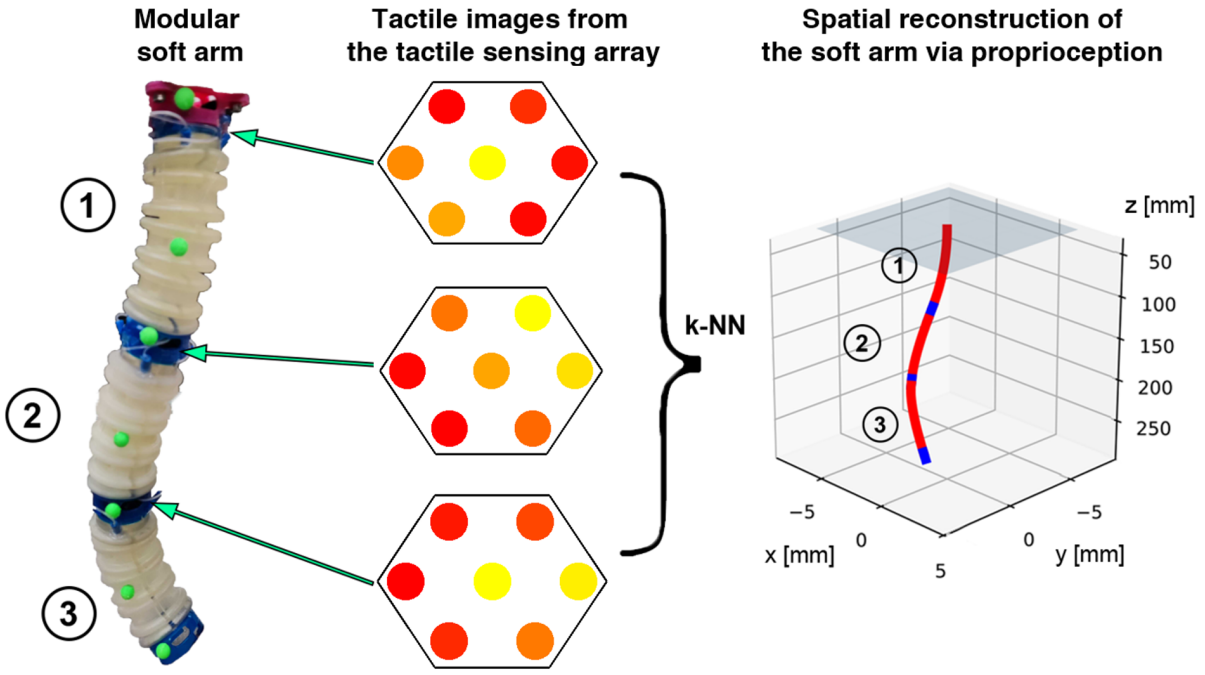


Figure 1.1: Overview of the proprioceptive soft robotic arm system. Each module is equipped with a sensing array where increasing brightness indicates higher sensor response. Given the readings, a trained k-NN is able to estimate the kinematic parameters which represent the spatial configuration of the soft arm under PCC assumption

soft robot to an integrated modular design of an omnidirectional bending pneumatic actuator. To capture critical bending motion of the actuator, 3D printed filtering pins were introduced to the actuator design to apply stress over the sensor. A piece of sensor was hosted inside the rigid part connecting two segments so the variation of the stress distribution over the top of the segment caused by the robot motion can be measured. Using a data-driven method, we were able to learn the correlation between the sensor responses and the soft robot postures and thus predict the spatial configurations with the sensor readings.

Moreover, it is worth noting that the integration of the sensing units does not affect the mechanical properties of the soft robotic arm. In addition, since the sensors are embedded on the top of the segment, they do not directly interact with the environment.

To summarise, the main contribution of the thesis is an novel proprioceptive sensing solution for modular soft robotic arms that does not affect their mechanical properties.

The thesis also contributes:

1. A modular method enabling fast arm assembling and sensor integration;

2. An omnidirectional actuator design for multi-material 3D printing.

The research findings have been summarised and reported in [Ouyang et al. [2022]] at IEEE International Conference on Soft Robotics (RoboSoft) 2022.

The thesis is structured as follows: In Chapter 2, we present a literature review of the proprioceptive soft robotic arms. We first discuss the challenges that need to be addressed to achieve proprioceptive soft robotic arm and then review the progress and limitations of existing proprioceptive sensing technologies. Chapter 3 explains the rationale and methodology of our solutions to tackle the challenges reviewed in Chapter 2. In Chapter 4, we present the details of the 3D printed multisegment soft robotic arm from design to fabrication and the corresponding actuation system. We also experimentally characterised the soft arm and the results are included. In Chapter 5, we brief how we endow the soft robotic arm with proprioception by correlating the stress distributions to the spatial configurations of the whole arm. Lastly, the main achievements are summarised in Chapter 6 where the limitations are also outlined.

2
Literature review

Autonomous robotic systems rely on integration of sensors. To achieve the closed-loop motion control, robots require proprioception to monitor their own shapes [Wang et al. [2018c]]. However, compared with their rigid counterparts, it is significantly more difficult to endow soft robotic arms with proprioception due to their infinite number of DoFs, deformable bodies and complexity in fabrication process [Tapia et al. [2020]]. In this chapter, we summarise the challenges in proprioceptive soft robotic arms and then introduce the current progress in tackling these challenges with various proprioceptive sensors and algorithms that interpret sensor responses as meaningful shape information.

As soft robotics is a relatively young field, there are very few multisegment soft robotic arms equipped with proprioceptive sensing ability. Therefore, we consider the soft continuum robots as one-segment soft robotic arms and include the corresponding sensorisation technologies and strategies endowing them with proprioception in the literature review.

2.1 Challenges in proprioceptive soft robotic arm

Traditional robotic arms possess a limited number of DoFs. Their movements are determined by the rigid joints that are connected by rigid links so the overall spatial configuration can be tracked by the sensors that monitor the state of each joint. In contrast, soft robotic arms can deform at all possible points of their soft bodies resulting in infinite number of degrees of freedom (DoF) [Wang and Chortos [2022]]. Following the same sensorisation strategy as with rigid robotic arms, there are attempts to tackle the challenge by embedding a high number of sensors in the body of the soft robotic arm [Yuen et al. [2018]; Farrow and Correll [2015]; White et al. [2017]]. However, when it comes to fabrication, it is a non-trivial task as manually fabricating soft sensors alone can be complex and the integration of these sensors may require a number of complicated steps [Totaro et al. [2017]]. Therefore, Muth et al. [2014] developed the corresponding fabrication technique to produce such sensors using 3D printers. Based on the works that fabricate soft robots using 3D printing techniques, Truby et al. [2018] have demonstrated the possibility to print a soft actuator along with conductive liquid-based sensors which allows direct fabrication of a soft sensorised actuator. As the number of sensors increases, it is no longer feasible to

fabricate the system with manual fabrication methods, and 3D printing techniques could be the solution to fabricate complex sensor network and the arm itself easily. However, it is ideal to minimise the number of sensors on-board, while still being able to measure the deformation of soft robots accurately. Tapia et al. [2020] presented a computational method to reconstruct the shape information of a soft continuum body with the minimal number of strain sensors possible. They stated that their approach could significantly simplify the process of fabrication.

Although there are a variety of soft strain sensors that have been developed to endow soft robotic arms with proprioceptive sensing ability and there are also works focusing on simplifying the fabrication process, soft and flexible sensors do not fully address the problems of proprioception [Scimeca et al. [2019]]. One main challenge of embedding soft strain sensors in soft robotic arms is that soft materials exhibit nonlinear and time-dependent materials properties, which demand the embedded sensors to accommodate for the compliance [Wang and Chortos [2022]]. Moreover, stretching and deformation of the soft robot may lead to changes in the relative position and orientation of the sensors with respect to the robot, which can cause noise or even failures of the sensing system [He et al. [2018]].

Apart from the embedded sensors, the soft robotic arm itself could be vulnerable to a variety of damages (cuts, tears, overloads, fatigue and etc.) which threats the overall durability of the proprioceptive soft robotic arm [Terryn et al. [2021]]. Since any wound on the soft robotic arm could lead to the failure of the whole system, it would be ideal to modularise the soft arm to enable maintenance and replacement of individual modules rather than the entire arm.

2.2 Progress in proprioceptive soft robotic arm

2.2.1 Proprioceptive sensing technology

Previous works have demonstrated the feasibility of using motion capture systems to retrieve the spatial configuration of soft robotic arms in open space [Katzschmann et al. [2019a,b]; Della Santina et al. [2020a]]. They are suitable for structured and controlled lab environments for proofs of concept. These systems are sensitive to environmental lighting or could be impaired by obstacles.

Driven by the demands of retrieving the configuration of soft robotic arms for closed-loop motion control, a wide range of soft and flexible sensors have been developed which enable the implementation of a mechanically compatible proprioception system for soft robots [Wang et al. [2018c]]. Although there is no unified framework to design a proprioceptive soft robotic

system due to the variety of the soft actuators and robots, proprioceptive sensors should generally meet the following requirements [Wang et al. [2018c]]:

1. Having low Young's modulus (<1 MPa) not affecting the mechanical properties of the soft robot. Traditional sensors such as encoders, inertial measurement units and strain gauges are rarely used with soft robots due to their deformable characteristics [Rus and Tolley [2015]].

2. Being resilient to endure large strain as the embedded sensor usually deforms with the robot [Homberg et al. [2019]].

3. Being robust against external mechanical stimulation [Wang et al. [2018c]].

4. During the fabrication process, the sensor should be integrated as a part of the soft body of the robots [Thuruthel et al. [2019]; Tapia et al. [2020]].

There are diverse sensing technologies that have been applied to address the problem of proprioception for soft robotic arms. In this section, we give an overview of these technologies and explain their mechanisms, as illustrated in Fig 2.1. We also discuss how these technologies are employed in soft robotic arms and evaluate their limitations based on the cases of implementations.

2.2.1.1 Resistive and piezoresistive sensors

As shown in Fig. 2.1(a) and (b), resistive and piezoresistive sensors measure the variations in the resistance caused by the changes in geometry or in resistivity of conductive materials [Stassi et al. [2014]].

Resistive sensors utilise conductive liquids that are embedded in elastomers or conductive polymers to realise a form of stretchable sensing Park et al. [2012]; Chossat et al. [2013]. These conductive liquids include low-melting point metal, metal alloys and ionic liquids [Wang et al. [2018c]]. Despite being a good conductor, liquid metals cannot work at temperatures that are lower than their melting point and their density is significantly larger than most elastomers [Helps and Rossiter [2018]]. By contrast, iconic liquids are relatively lighter and cheaper but have poorer conductivity and long-term stability because of electrolysis [Bahramzadeh and Shahinpoor [2014]]. Resistive sensors are highly stretchable and high performance [Zhang et al. [2017]; Kim et al. [2020]]. They have already been integrated into several single-segment soft robotic arms capable of multi-directional or omnidirectional bending motions [Russo et al. [2015]; Morrow et al. [2016]; Wurdemann et al. [2015]; Zhao et al. [2021]]. In these works, resistive sensors

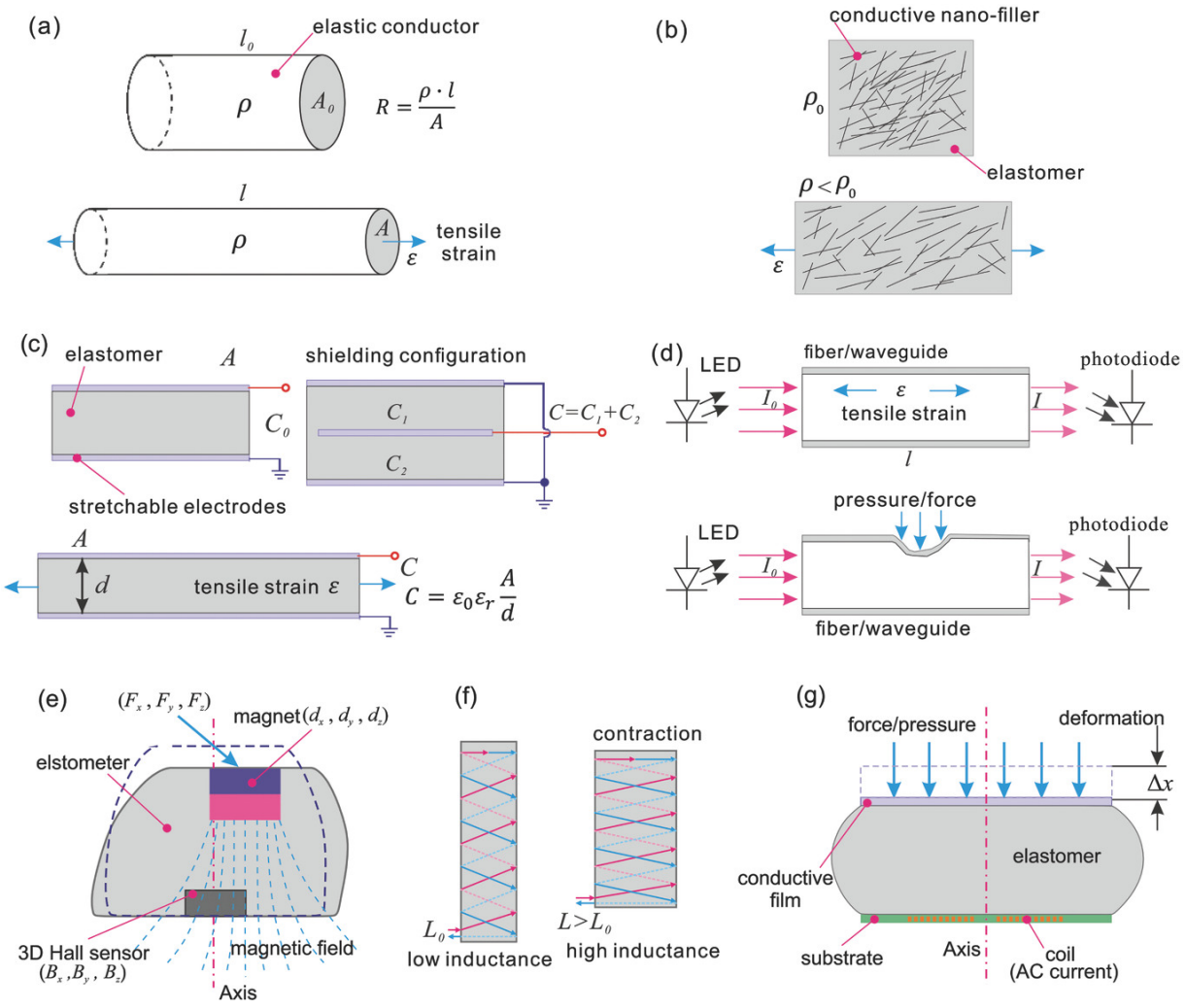


Figure 2.1: Mechanisms for proprioceptive sensing [Kim et al. [2021]]. a) Resistive sensor b) Piezoresistive c) Capacitive sensor d) Optical sensor e) Magnetic sensor f) Inductive "Smart braid" for McKibben actuator g) Inductive sensor

functioned as stretchable strain sensors that measure the bending curvature of the soft robotic arms. Nonetheless, the integration of these sensors is a non-trivial task. Microchannels are required to direct the conductive liquids which poses challenge to fabrication. Therefore, a robust design of the overall system is needed to ensure rigorous interconnections between the liquid channel and solid wires [Secor et al. [2018]]. On the other hand, these channels are fragile which leads to the risk of leakage [Chossat et al. [2013]].

Piezoresistive sensors exploit elastomeric composites filled with conductive fillers such as nanoparticles, wires or flakes [Stassi et al. [2014]]. When strain is applied, both their resistivity and geometry change as shown in Fig 2.1(b). The mechanical and electrical properties of nanocomposites are tunable [Stassi et al. [2014]]. Unlike resistive sensors, conductive nanocomposite-based sensors do not require complicated fabrication process [Ma et al. [2021]].

These sensors have been integrated on various soft robots including soft robotic arms to measure the bending curvatures [Yamamoto et al. [2007]; Kure et al. [2008]; Cianchetti et al. [2012]; Truby et al. [2020]]. The main downsides of piezoresistive sensors are large hysteresis, long recovery time, slow responses, and nonlinearity [Amjadi et al. [2016]]. Moreover, there is a trade-off between stretchability and sensitivity, since high conductivity requires high filler ratio, while this leads to a high stiffness and low stretchability [Park et al. [2015]].

2.2.1.2 Capacitive sensors

Capacitive sensors measure the variations in the capacitance when the elastomer deforms [Viry et al. [2014]] as shown in Fig. 2.1(c). So far, past works have developed several stretchable conductive materials such as conductive fabric, nanocomposites, conductive polymer as stretchable electrodes [Wang et al. [2018c]]. These sensors show high sensitivity, rapid responses and good linearity [Viry et al. [2014]]. Because of their performance and linearity, capacitive sensors have been well developed as soft strain sensors to measure the bending curvature of soft bodies [Farrow and Correll [2015]; Lucarotti et al. [2015]; Dawood et al. [2019]] which shows the potential to be integrated with soft robotic arms.

However, Wang et al. [2018c] reported that capacitive sensors are sensitive to environmental contaminants such as oil, dust, liquid and vaporous water and can be affected by conductive objects. To address these problems, shielding is required to protect the sensors which complicates the fabrication process [Maddirala et al. [2022]]. In addition, both pressure and strain can cause variation in the capacitance so they are difficult to decouple.

2.2.1.3 Optical sensors

Optical strain sensors measure the light variations such as intensity and frequency caused by the strain of the transmission medium [Yun et al. [2014]; Zhao et al. [2016]] as shown in Fig. 2.1(d). Light intensity measurement is the most common mechanism of this type of sensor which includes a light source, a photodetector and light transmission medium. These sensors are highly flexible while being insensitive to electromagnetic interference and environmental contaminants [Zhao et al. [2016]]. They have been integrated with an omnidirectional soft robotic arm to measure its bending angle and direction [Sareh et al. [2015]; Scharff et al. [2021]].

In addition, to tackle the challenge of perceiving non-uniform deformations, especially at high curvature, Aljaber et al. [2022] developed a multi-point waveguide sensor to detect the bending behaviour at multiple points of a soft pneumatic actuator. By measuring the

variations in the waveguide's length at different points, the bending curvature of the soft actuator was accurately estimated.

For pneumatically driven soft robotic systems, embedded strain sensors are usually susceptible to several stimuli such as bending, external contacts and actuation pressure. Therefore, it is important to decouple the deformations and the forces. Godaba et al. [2020] proposed to address this challenge by employing a sensor based on abraded optical fibres that is insensitive to normal forces exerted by external forces or internal pressure.

Nevertheless, the fabrication process is usually expensive and complex due to the complicated electronics and the rigidity of photodetectors that renders the integration difficult. What's more, the relatively limited stretchablility of optical sensors is also a main barrier for integrating these sensors in soft robotic arms [Zhuang et al. [2018]; Wang et al. [2016a]].

2.2.1.4 Magnetic sensors

Similar to optical sensors, magnetic strain sensors consist of a magnetic source, a magnetic field sensor (Hall-effect sensor) and a soft medium [Jamone et al. [2015]; Wang et al. [2016b]], as shown in Fig. 2.1(e). As the soft medium deforms, the readout of the magnetic field sensor varies since the relative position and orientation of the sensor change with respect to the magnetic source. Based on this mechanism, magnetic sensors are compact, cheap, high sensitive and easy to use [Wang et al. [2018c]]. They have been employed to measure the bending curvature of multi-directional soft robotic arms [Luo et al. [2017]; Ozel et al. [2015]; Visentin et al. [2020]].

On the other hand, magnetic sensors are inherently prone to external interference caused by environmental magnetic field variations [Wang et al. [2018c]].

2.2.1.5 Inductive Sensors

Inductive sensors measure the variations in the inductance to monitor the deformation of soft robots [Lazarus and Bedair [2018]; Wang et al. [2018b]] as shown in Fig. 2.1(g). Felt et al. [2017] developed an inductance-based soft sensor for McKibben muscles by wrapping stretchable helical coils around the fibre-reinforced braid (see Fig. Fig. 2.1(f)). The contraction of the coils can be represented by the variations in inductance. Using this principle, Felt et al. [2019] have successfully developed the inductive sensor for measuring the bending curvature of an omnidirectional soft robotic arm. The main disadvantage of inductive sensors is the complexity of signal conditioning electronics Wang et al. [2018a].

2.2.1.6 Non-strain sensors

So far, we have reviewed a variety of soft strain sensors that have been developed to be embedded in the soft bodies to measure the deformations. Since they become a part of the body of the robots, they have to satisfy the basic requirements to make the integration possible such as being soft and compliant, being able to endure large strain, and being embedded during the manufacturing process. However, there are proprioceptive sensing technologies that do not require embedding sensors within soft bodies as they do not directly measure the strain. With these approaches, some problems of sensor integration and fabrication can be avoided and they can remain functional when the robot is experiencing external forces.

Su et al. [2020] claimed that they have realised proprioception for their soft bending actuator with pressure sensors that measure the actuation inputs. Based on Boyle's law, they modelled the relationship between the actuation inputs and the deformation of the actuator. Given the actuation inputs, it was possible to estimate the posture of the actuator. However, this approach is only able to estimate the quasi-static state of the soft robot due to hysteresis and slow response time.

The challenge of sensing soft robot shape can be formulated as estimating tip positions when the soft robot is single-segment. Hughes et al. [2020] proposed to mount Inertial Measurement Units (IMUs) on the tip and end of a soft continuum manipulator to perceive its 3D shape.

Another approach has been presented by [Scimeca et al. [2019]] where a capacitive sensor array was integrated on the top of a soft actuator to measure the stress distribution which was correlated with the tip position of the actuator using data-driven method. This method has been demonstrated on a tendon-driven single segment soft robot but it remains unknown whether this method is applicable to soft robotic arms that are pneumatically driven and consist of multiple segments.

Camera-based motion capture systems have demonstrated its feasibility to retrieve the spatial configuration of soft robotic arms and provide feedback for posture control [Katzschmann et al. [2019a]; Della Santina et al. [2020a]; Satheeshbabu et al. [2020]; Vitanov et al. [2020]]. However, this method is infeasible in dark environment or unstructured environment where obstacles could impair the visual feedback. Instead of employing external cameras, Rosi et al. [2022] equipped a multisegment soft robotic arm with monocular cameras where a camera is attached to each segment. By using SLAM algorithms to estimate the pose of cameras, the postures of the corresponding segments were estimated and hence the shape of the multisegment soft robotic arm was retrieved.

2.2.2 Sensor data interpretation

Besides the acquisition of the sensory feedback, it is also vital to interpret the data to describe the complex deformations of the soft body of the robot. In this section, we review different approaches to analyse and exploit raw data from proprioceptive sensors.

2.2.2.1 Model-based approach

For a pneumatically driven soft robotic arm, pressure sensors are essential for providing feedback for low-level pressure control. An intuitive approach to realise proprioception is to utilise pressure sensors measuring the air pressure to compute the change in the chamber volume. According to Boyle's law, the absolute pressure exerted by ideal gas is inversely proportional to the volume. Based on Boyle's law Su et al. [2020] managed to calculate the axial displacement of the pressurised chamber of their soft robot given the actuation pressure. However, this approach only works in quasi-static conditions and neglects the bending of the chamber.

Instead of pressure sensors, a more common solution is to utilise soft and flexible strain sensors to measure the local deformations and then compute the overall spatial configuration of the soft robotic arm. This method usually requires a high number of sensors which are either embedded in or attached to the soft body of the robot. By converting the sensor feedback into local extensions, Wurdemann et al. [2015]; Farrow and Correll [2015]; Felt et al. [2019] calculated the characteristics of a visual centre-line and then computed the corresponding parameters under piecewise constant curvature (PCC) assumption. PCC assumption is a simplified approach that approximates the soft robotic arm with finite circular arcs and each of them is described by a set of parameters that could represent the shape information [Russo et al. [2015]].

Furthermore, previous studies have demonstrated that various sensor responses could be correlated to PCC parameters. Visentin et al. [2020] utilised a single Hall effect sensor to reconstruct the shape of their soft robotic arm. By placing the magnet in the robot body, the magnetometer could monitor the relative motion of the magnet. With the position of the magnet, the curve between the magnetometer and the magnet was plotted and hence the kinematic parameters was computed to describe the shape of the robot. With Inertial Measurement Units (IMUs) sensing 3-axis acceleration and angular velocity of the soft robot tips, Hughes et al. [2020] measured the centre-line characteristics of their soft robot and converted them into PCC parameters. Rosi et al. [2022] proposed to attach cameras to a soft robotic arm which provided cues for localisation and tracking. The camera poses were estimated and converted into the parameters of a PCC model who described the kinematics of the soft arm.

When the soft robot is subjected to an external force, PCC assumption is no longer viable [Visentin et al. [2020]]. Sadati et al. [2020] proposed a shape and tip force estimation method relying on Cosserat rod theory and the readings from a force sensor mounted at the base of a one-segment soft robotic arm. However, they focused on estimating the tip position and the force applied while the reconstruction of the overall shape configuration of the soft arm was not validated.

2.2.2.2 Data-driven approach

Similar to [Wurdemann et al. [2015]; Farrow and Correll [2015]; Felt et al. [2019]], Truby et al. [2020] employed soft strain sensors for their multisegment soft robotic arm. Rather than finding the characteristics of the centre-line, they directly learned the relationship between the PCC parameters and the strain sensor responses using a long short term memory (LSTM)-based neural network which avoided the error in estimating the centre-line and dramatically increase the efficiency and accuracy of data interpretation.

When dealing with simple single-segment soft robotic arms, the proprioceptive sensor feedback could be interpreted as the tip position of the robot. For example, Scimeca et al. [2019] employed a simple feedforward neural network to map the raw tactile data to the Cartesian coordinates of the tip of a single-segment tendon-driven soft robot. Similarly, Zhao et al. [2021] learned the mapping between a piezoresistive sensor readings and the tip position which represents the spatial configuration using multilayer perception (MLP) neural networks. If the soft robot is capable of ominidirectional bending, it could be considered as a soft continuum joint whose spatial configuration could be converted into a rigid transformation represented by a rotation matrix and a translation vector and the correlation was learned by a LSTM model [Scharff et al. [2021]].

In conclusion, data interpretation algorithms based on constant curvature assumption are highly popular in the field of soft robotic arms. They provide an analytical description of the soft robot's shape, even if the robot is multisegment. Although this assumption is prone to external forces since the bending moment is no longer constant [Visentin et al. [2020]], we do not consider external contacts in this project so PCC assumption is applicable. It has also been demonstrated that data-driven methods are powerful in obtaining the mapping between the sensor readings and model parameters which represent the overall spatial configurations of soft robotic arms.

3
Motivation and Methodology

In the Chapter 2, we have reviewed the recent research progress of proprioceptive soft robotic arms and their limitations. In this Chapter, we give an overview of our approach to tackle the existing challenges in the field of proprioceptive soft robotic arms. Fig. 1.1 shows a three-segment soft arm with embedded sensor feedback which is used to reconstruct the shape of the arm using a trained k-NN. A hexagonal sensing array is embedded within the joint of each segment to measure the stress distribution when the robot is moving. Fig. 1.1(middle) show the output of the three sensors, where brighter colour corresponds to higher sensor response. Fig. 1.1(right) illustrates that the soft robotic arm posture is reconstructed using the output of a trained k-NN regressor. The k-NN regressor takes the measurements of the sensors as the input and outputs the kinematic parameters which represent the soft robot spatial configuration.

3.1 Modular soft robotic arm design

3.1.1 Omnidirectional bending soft actuator

In this thesis, we aimed to explore the shape reconstruction of a soft robotic arm in the 3D space so we developed a soft robotic arm comprising multiple omnidirectional soft actuators. As demonstrated in [Balak and Mazumdar [2020]; Fras et al. [2020]; He et al. [2021]], omnidirectional bending can be realised by having three asymmetric chambers performing antagonistic bending motion. Therefore, we adapted the design presented in [He et al. [2021]] where apart from the three chambers to achieve omnidirectional movements, beam constraints are introduced to mitigate the undesired radial expansion. The rationale behind the design of the internal constraint structures is explained in Chapter. 4. Since no other constraint structure such as reinforcement fibre is used, additional procedures are not required to fabricate such omnidirectional bending soft actuator so He et al. [2021] reported that their design can be directly manufactured with single material 3D printing technology. Although we adopted an existing design to minimise the fabrication procedures involved to fabricate our soft robotic arm while being able to achieve omnidirectional bending motion, we iteratively improved the original design by introducing bellow-like structures to overcome the stretching capability limitation of the 3D printed material as detailed in Chapter 4. Furthermore, the original design was fabricated using a material that is

only available for single material DLP type 3D printers so we also adapted it for the materials that are available for the multi-material 3D printer we used in this project.

3.1.2 Modular design and fabrication

With omnidirectional bending actuators who function as basic modules, a multisegment soft robotic arm can be formed by gluing together multiple actuators as in [Katzschmann et al. [2019a,b]; Della Santina et al. [2020b]; Jiang et al. [2021]]. However, following this method, the integration of the proprioceptive sensors has to be completed before the fabrication of the soft robotic arm and the possibility of appending or removing segments is constrained. Furthermore, Terryn et al. [2021] show that the soft materials used for soft robot fabrication are prone to different types of damage, for example overloads, fatigue, and interfacial debonding. Joining soft segments together with glue hinders the replacement and maintenance of the soft robot system. Therefore, we adopt a modular approach as shown in Fig. 1.1(left) - each module consists of an omnidirectional bending actuator (white) and rigid joint features (blue) that can connect to other modules to form the soft robotic arm. These joints can be locked or unlocked by simply rotating them clockwise or counter-clockwise so the modules can be replaced easily. They do not only secure the interconnection between modules, but they also host the sensors to prevent detaching during robot motions.

There are several components that need to be fabricated for one single module: the omnidirectional soft bending actuator, the filtering pins (the rationale of adding the pins is explained in the next section) and the rigid joint features. Because of the internal constraint structures, it could be an non-trivial task to manufacture the actuators using traditional casting technique as it demands complicated mould design and manual work. Therefore, we fabricated the actuators and the pins together using 3D printing technique that is able to create complex 3D geometries easily. Due to the complexity in fabricating the rigid joints and the actuators separately and assembling them, we selected multi-material 3D printing over single material 3D printing so the rigid parts can be manufactured along with the actuator and the pins without further integration steps.

A Stratasys J735 Polyjet printer was employed in this project to fabricate the soft modules. It took around 3.5 hours to print one module and it took another 6 hours to post-process the printed parts to remove the support materials in a rinsing tank. The sensing units were manufactured by the Oxford Soft Robotics Lab and each costs around £15. Thanks to the modular design, by locking the joints the modules can easily interconnects. When the joints were unlocked, the

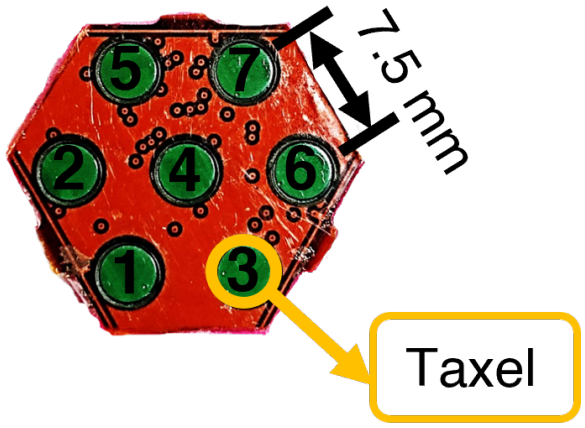


Figure 3.1: CySkin sensor used in this project. Each sensor hosts 7 taxels which are numbered from 1 to 7. The positions of the numbers indicate the layout of the taxels.

sensing units could be directly placed within them, and the cables can be pulled through the holes on the wall. A detailed view of the joint design can be found in Fig. 4.1.

3.2 Soft robotic arm proprioception

Considering the limitations of soft strain sensors, we followed the approach of [Scimeca et al. [2019]], where a piece of sensing array was used to capture the stress distribution over the top of a soft robot to realise proprioception. In this thesis, we extended this approach to endow a multisegment soft robotic arm with proprioceptive sensing ability. The sensor used in this project (namely *CySkin* [CySkin [2022]]) is an updated version of the tactile sensing technology presented in [Schmitz et al. [2011]]. It is a flexible PCB hosting 7 capacitive based transducers (taxels) evenly spaced of 7.5 mm as shown in the Fig. 3.1. Each taxel measures the corresponding magnitude of stress over itself so 7 taxels together measure the stress distribution over the plane to which it is attached. The details of the CySkin sensor can be found in Chapter 4.

It is worth noticing that in [Scimeca et al. [2019]] the CySkin sensor was directly attached to the flat top plane of the tendon-driven soft robot but considering the differences in the actuation methods, we added 7 cylindrical pins on the top of the omnidirectional bending actuator to filter and enhance the sensor responses. Besides, the rigid joints were added as the shell to isolate the CySkin sensor and the pins from the external environment so physical contacts do not interact with the sensors which improves the durability of the system.

A three-segment soft robotic arm was used to demonstrate the proprioception. It comprises three soft modules and three pieces of CySkin sensing arrays. However, the relationship between the sensor responses and the soft robot posture is difficult to model so we obtained the correlation

between the sensor responses and the soft robot pose through a data-driven approach. What's more, the pose of the robot was represented by its tip position in the original work. In this project, we are aiming to estimate the entire shape information of a three-segment soft robotic arm whose pose cannot be fully represented by Cartesian coordinates of its tip. Therefore, we parameterised the spatial configurations of the soft robotic arm under Piecewise Constant Curvature assumption so we reframed the problem of retrieving the shape information of the soft robotic arm by estimating the kinematic parameters of it. We used a motion capture system to record the positions of the visual markers attached to the body of the soft robotic arm which can be converted into kinematic parameters. With the motion capture system and a pneumatic actuation system supplying driving pressure to the soft robotic arm, we were able to drive the soft robotic arm to arbitrary poses in open space and record the corresponding sensor responses and the kinematic parameters. As a result, we trained a k-NN regressor mapping the CySkin sensor responses to the kinematic parameters which represent the spatial configuration of the soft robotic arm and thus we were able to accurately estimate the whole shape information of a three-segment soft robotic arm given the sensor readings.

4
Modular soft robotic arm

In this chapter, we present the details of a modular soft robotic arm that is designed for direct 3D printing, omnidirectional bending, and the integration of the in-joint tactile sensing arrays. The basic actuator design is adapted from [He et al. [2021]], where the concept of internal beam constraints are employed to control the bending motion and mitigate the undesired radial expansion.

4.1 Module design

Terryn et al. [2021] suggests that the compliant materials used for the construction of soft robots are prone to damage, such as fatigue, overloads, interfacial debonding, and cuts, tears and perforations by sharp objects. The durability of the overall proprioceptive soft robotic arm system can be improved if it is modular and allows a single module to be replaced rather than replacing the entire soft arm when a module is damaged. Furthermore, by embracing the concept of modular design, we focus on the design of one single module rather than the entire multisegment soft robotic arm since the arm consists of identical modules. Each module is an omnidirectional bending actuator with the cylindrical pins on its top to filter the tactile sensor reading to achieve proprioceptive sensing (See Fig. 4.1).

He et al. [2021] proposed a design of omnidirectional bending soft actuator driven by air pressure. Since it contains beam elements (See Fig. 4.1a) functioning as internal constraints to limit the radial expansion of the body of actuator when it is inflating, it does not require extra steps to add external components to constrain the undesired expansion. Therefore, it is suitable for direct 3D printing. However, the original prototype was fabricated with a rebounding resin with Shore hardness 25A using a single material 3D printer, while we employed multi-material polyjet 3D printing to fabricate the rigid joint features along with the actuator to avoid additional integration steps and the softest material that is commercially available to polyjet multi-material 3D printers is Agilus 30 whose Shore hardness is 30A. Hence, we modified the design: 1) for the 3D printing material with a higher Shore hardness; 2) to achieve a larger bending angle with relatively low driving pressure. In addition, the original design consists of three enclosed chambers to achieve omnidirectional bending. For the sake of the interconnections between

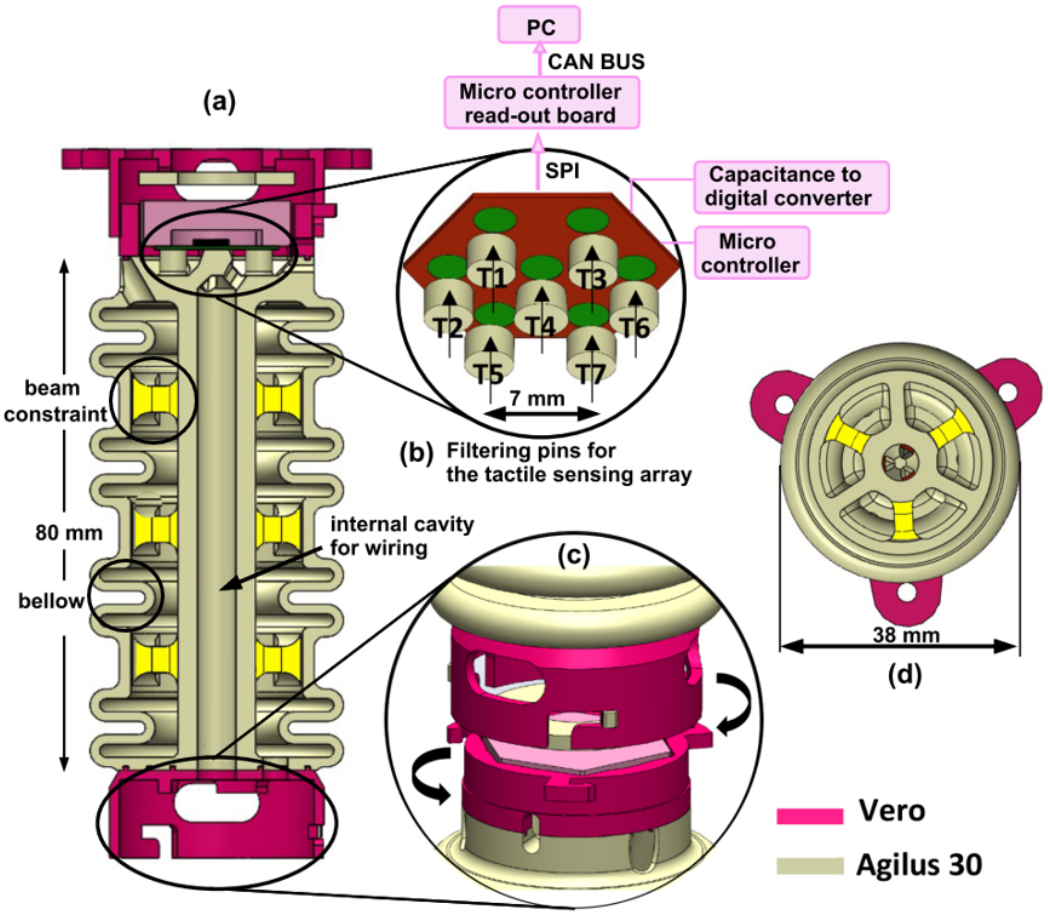


Figure 4.1: Overview of soft robotic arm module design (Colours represent the material types and constraint beams are highlighted in bright yellow): a) An axial view of the segment. The tactile sensing array is mounted on a hexagon holder and placed at the joint of the actuator. Three beam constraints can be seen in each chamber. b) Detailed view of the sensing unit and the forces exerted by the pins on top of the segment. The sensing unit is placed between the pins and its base (Pink). 7 soft pins are added as morphological filters to filter the tactile information, aligned with the 7 sensing taxels. c) Close view of the joint connection design showing how the relative position of two connected segments can be locked. Small cubes are printed on the surface with Agilus 30 ensure a tight connection d) Radial view of the module. It can be observed that each chamber takes up 120 degrees.

multiple actuators to form the soft robotic arm, a central channel was added to the original design so the pneumatic wires can pass through to connect to other modules. The length and radius ratio of the actuator were also based on [He et al. [2021]] and adapted to suit the size of the tactile sensing array. In order to focus on the optimisation of the internal structures, the lengths of the actuators were fixed to 100.5mm (rigid parts included).

W iteratively improved our design based on the results of FEM simulations, namely the bending angle achieved at 15 kPa and the safety factor. Agilus 30 is a soft material whose mechanical properties are highly nonlinear, hence we used a 3rd degree Ogden model to describe its hyperelastic behaviours. The Quasi-static Ogden hyperelastic material model parameters

are summarised in Table 4.1 [Abayazid and Ghajari [2020]].

Table 4.1: Ogden Quasi-static hyperelastic maeterial parameters for Agilus 30

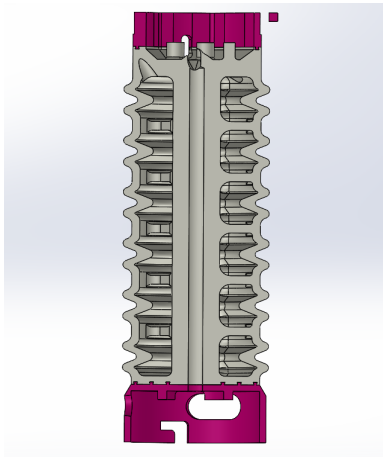
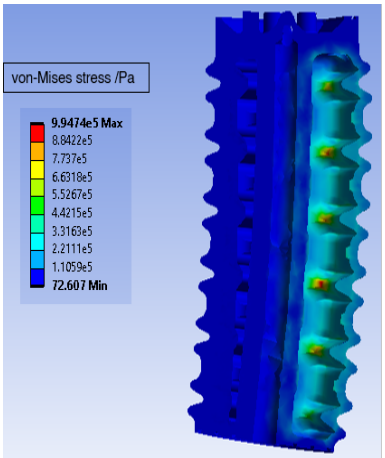
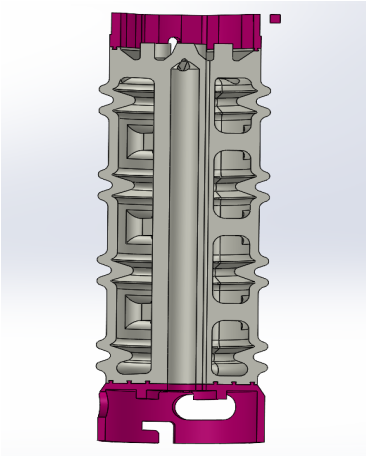
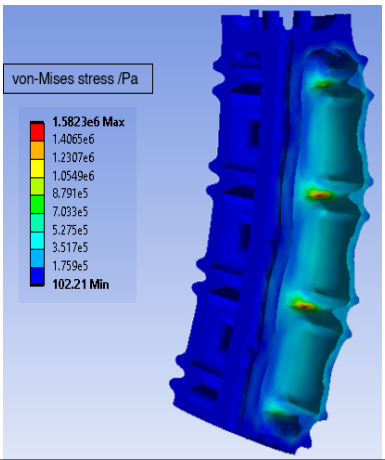
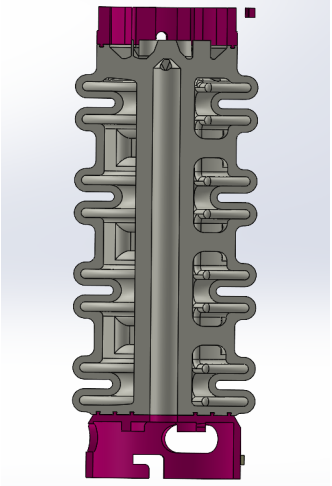
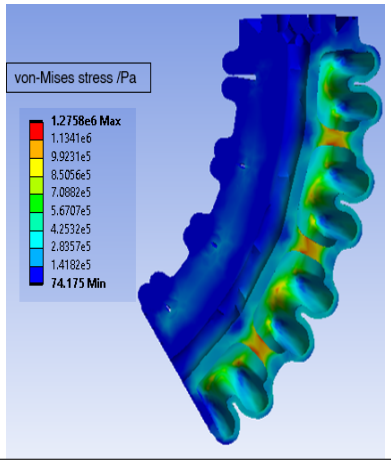
Material Constant	Value
μ_1 [MPa]	0.2127
α_1	1.3212
μ_2 [MPa]	0.0375
α_2	4.318
μ_3 [MPa]	-0.001
α_4	-1.0248

With the material constants for Agilus 30, we were able to simulate the material properties of Agilus 30 using 3rd degree Ogden hyperelastic model in Ansys FEM simulation software. Due to the fact that FEM simulation could be computationally expensive and time-consuming, we tend to minimise the size of our FEM models. Therefore, we evaluated the performance of our single module designs rather than the whole arm, under a fixed maximum driving pressure as shown in Fig. 4.2. The module is capable of omnidirectional motion, but we pressurised one chamber and compared the corresponding bending angle in one direction (See 4.2(b)). The upper rigid joint is fixed (See Fig. 4.2(a)) and hence the top plane of the actuator is fixed as well. For a more realistic simulation, standard earth gravity was added to estimate how much the actuator can bend while carrying its self-weight.

4.2(c) shows an example of FEM simulation results. Bending angle θ is derived from the angle between the two end-plates. In engineering design, it is important to ensure the component is designed to bear more loads than its expected operating loads, thus safety factor is defined as the ratio of the ultimate stress of the component material to the working stress. In our case, the safety factor was the ratio of the tensile strength value given by [Stratasys [2022a]] to the maximum von Mises stress given by the simulation results. There is no fixed range of this safety factor; we usually applied a 1.5 factor [Burr and Cheatham [1995]].

As can be seen in the top row of the Table. 4.2, the original design has 5 internal constraint beams within each chamber which mitigates the radial expansion when the chamber inflates. However, under 15kPa, the actuator was not able to bend to a desirable large angle in the FEM simulation. Therefore, we reduced the number of internal constraint beams to 3 per chamber in order to achieve a larger bending angle but this led to a drop in the value of safety factor (See Table. 4.2(middle)). Finally, we introduced the bellow features to the design. As a result, we observed a notable increase in both maximum bending angle and safety factor and hence it became our final design for the main body of the soft pneumatic actuator.

Table 4.2: Iterative design of the soft module and their performances based on FEM evaluation

Cross-section view	Performances	Key features
	• Maximum bending angle: 10.05 degrees • Safety factor: 3.116 	• Taken from [He et al. [2021]] but added central channel • 5 internal constraints within each enclosed chamber • No failure observed under 15 kPa
	• Maximum bending angle: 23.64 degrees • Safety factor: 1.959 	• 3 internal constraints within each chamber for larger bending angle • Failure observed in the areas where the von-Mises stress reaches the maximum (the bellows) after repetitive inflation and deflation
	• Maximum bending angle: 47.71 degrees • Safety factor: 2.430 	• Introduced bellow structure for better bending performance and a larger safety factor • No failure observed under 15 kPa

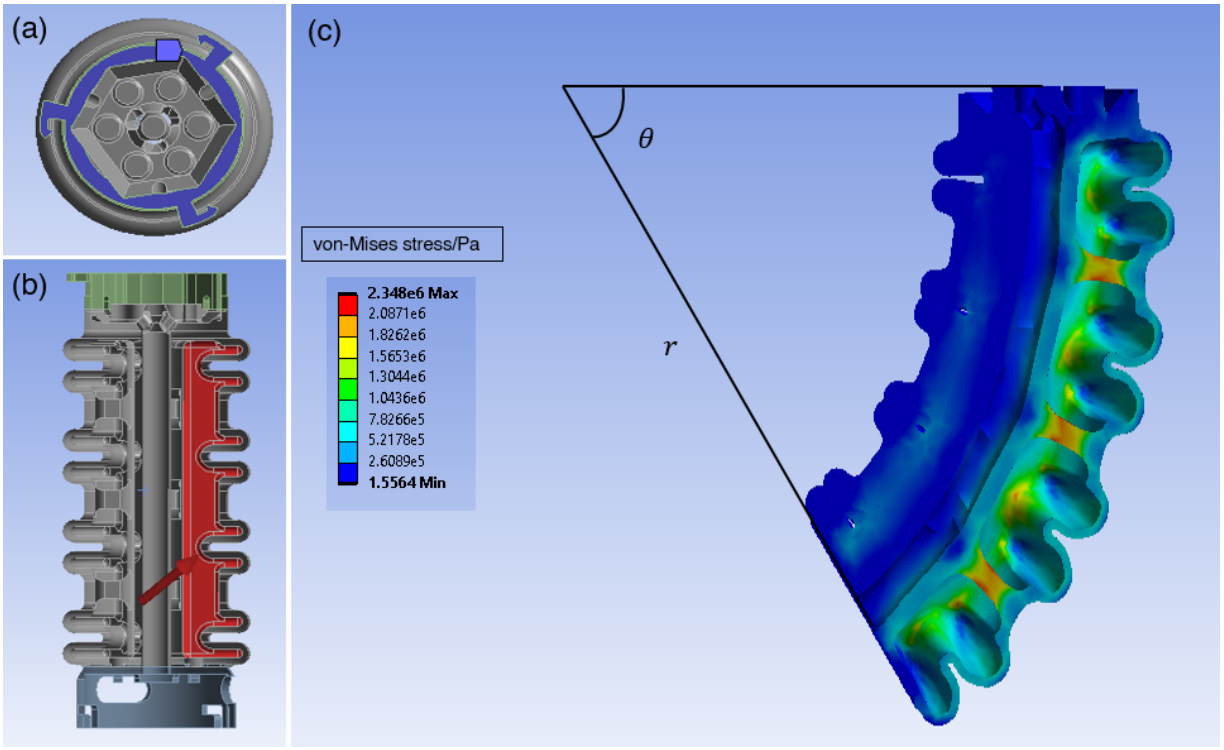


Figure 4.2: Overview of the FEM simulation setup and example results: (a) Fixed support (b) Pressurised chamber (c) Cross-section simulation results: bending angle θ and von-Mises stress (indicated by the colour), when subjected to 15 kPa driving pressure.

The CySkin module is composed of a flexible PCB containing 7 taxels evenly spaced of 7.5 mm, as shown in Fig. 4.1(b) and Fig. 3.1. A conductive fabric covers the CySkin sensor, acting as a ground plane. The variations in the stress distribution over the sensor causes deformations of the dielectric layer. A 16-bit Capacitance to Digital Converter (CDC) and a microcontroller are embedded on the back of the PCB, recording the changes of capacitance caused by the deformation of the ground plane.

Considering the location and geometry of the 7 taxels on the hexagonal shaped CySkin sensor, 7 cylindrical features were added to filter and augment the sensor readings to capture the stress distribution on the top when the soft robot moves to a quasi-static state. The sensor responses were used to create a model mapping the CySkin output with the spatial configuration of the soft robot. The details are included in the Chapter 5.

The tactile sensing array was embedded within the 3D printed housing between the connecting joint of two modules. The housing of the tactile sensing array also functioned as the connector to attach the two neighbouring modules. As can be seen in Fig. 4.1 (c), two modules can be connected or disconnected by rotating the connector clockwise or anticlockwise. Small soft cubes were printed on the surface of the bottom connector ring to ensure a tight connection.

The soft module, as well as the whole modular soft robotic arm, were fabricated with a Stratasys J735 polyjet 3D printer, where multiple droplets of uncured material were deposited and blended and cured by UV light. The main body of the module (the pneumatic actuator) was printed with Agilus 30 (a soft and rubber-like material with a quoted tensile strength of 2.1-2.6 MPa and a Shore hardness of 30A [Stratasys [2022a]]). The joints were printed with Vero (a rigid plastic-like material with a quoted tensile strength of 50-65 MPa and a Shore hardness of 83-86D [Stratasys [2022b]]). The monolithic fabrication solution allowed the soft and rigid parts to be combined securely during the actuation. The joints were designed to be rigid to ensure tight interconnections between soft modules and provide housing for the sensing units. They could become a failure point due to the lack of compliance when subjected to external forces. However, the investigation of the effects of external forces is beyond the scope of this project and the joints could be redesigned or protected by soft materials for the future work.

All modules were post-processed to remove the internal support material in a tank (GEMINI SSR-550) rinsed with support removal solution (0.02 kg/L Sodium Hydroxide and 0.01 kg/L Sodium Metasilicate). After post-processing, the average net weight of the module is around 53g.

4.2 Experimental setup

In this section, we introduce the hardware systems we used to operate and characterise the bending performance of soft robotic arm. The hardware setup includes: 1) a pneumatic actuation system regulating the air pressure within each chamber and driving the motion of the module and the soft robotic arm; 2) and a motion capture system that provides the ground-truth spatial configurations of the soft bending module and the soft robotic arm. In Chapter 5, this setup is employed to collect data and validate the proprioceptive ability of the soft robotic arm.

4.2.1 Pneumatic actuation system

To operate a three-segment soft robotic arm, a pneumatic actuation system was built to control the multiple chambers independently. Since the soft arm is composed of three soft modules, each one having three chambers, the control system needs to control the actuation pressure of 9 chambers in total. For the simplicity of control, we designed the pneumatic actuation system to be able to control the segments separately. As showed in Fig. 4.3, representing the control system of a single segment, three 60 mL syringes were connected to the three chambers through silicone pipes. The plunger flanges of the syringes were driven by three stepper motors which allowed precise control of the pressures inside the corresponding chambers.

A pressure sensor (ADP51A11, Panasonic, Japan) was used to measure the pressures inside the chambers up to 40kPa. Before the operation of the soft robotic arm, all the barrels of the syringes were fully loaded while the solenoid valves (12V DC, Yosoo, UK) were open so the pressure sensor readings could be initialised. All components used for actuating one module were connected to an Arduino Mega 2560 board, implementing a PI controller that regulated the pressure inside the chambers by controlling the movements of the motors. The desired actuation pressure was commanded from an external computer to the Arduino through serial communication.

4.2.2 Motion capture system

As can be seen in Fig. 4.4, the green visual markers were attached to the soft robot body. The 3D coordinates of the markers (attached to the top, middle and bottom of each module) were captured using two cameras (C270, Logitech). The positions of the markers were then used to compute the kinematic parameters which describe ground-truth spatial configuration of the soft robotic arm. This system captured postures when the soft arm reached quasi-static states and dynamic effects were not captured.

The webcams were calibrated using OpenCV camera calibration tool which computed the camera matrix and distortion coefficients. Sources of error included the oblique projection, the lens distortion and random errors in the marker position. As a result, the estimation error for coordinate measurement was approximately 0.5 mm when tracking the coloured markers that were placed in different positions at steady state.

4.2.2.1 Constant curvature kinematic model

The spatial configuration of a soft module was approximated using a Constant Curvature (CC) model (as shown in Fig. 4.5) so the posture of the module could be described using three parameters: the arc radius r, the arc angle θ and the angle ϕ of the plane where the arc was defined in the 3D space [Webster III and Jones [2010]]. When it comes to characterising the bending performance of the soft robot, we evaluated the arc angle θ that indicates how much the robot bends.

Therefore, given the coordinates of the start, the midpoint and the end of a curve in the 3D space, the kinematic parameters can be computed using Algorithm. 4.1 [Alexiou [2019]].

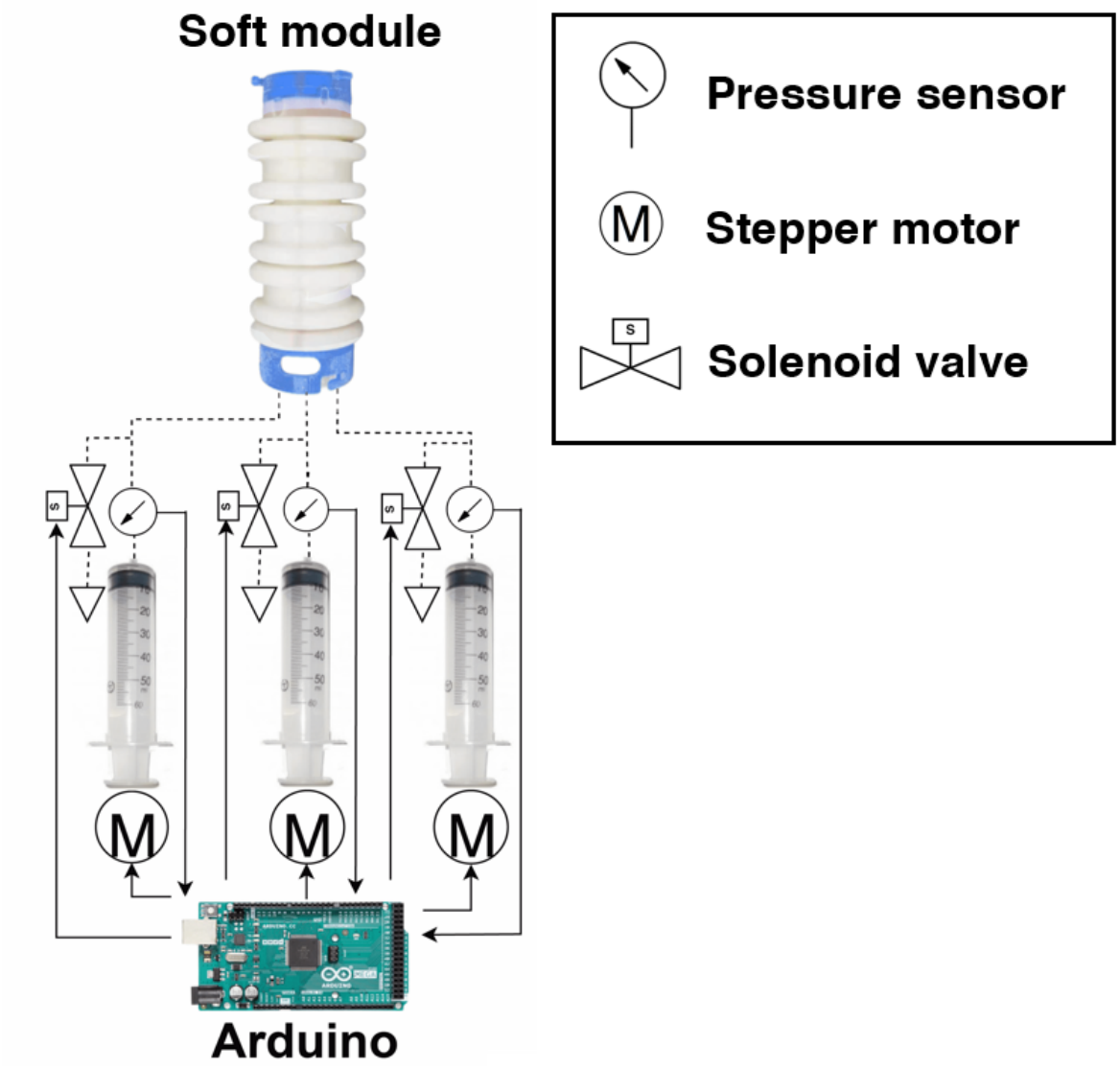


Figure 4.3: Schematics of the pneumatic actuation system for controlling one soft module (The dashed lines represent the pipes and the solid lines indicate signal communications). Each chamber of the module is connected to a solenoid valve, a pressure sensor and a syringe by silicone pipes. The syringe is driven by a stepper motor who is controlled by an Arduino board to deliver air pressure to the corresponding chamber. The pressure sensor measures the pressure and sends the reading to the Arduino. The solenoid valve is used to ventilate the syringe when needed. Three interchangable systems are used to control the three-segment soft robotic arm.

4.3 Experimental characterisation

In the Module design section, we have evaluated the bending performance of our modules in a FEM simulator. This section describes the experiments conducted to characterise the performance of our final design, testing both the repeatability and the bending angle that is converted from the marker positions captured by the motion capture system using Algorithm. 4.1.

The experiment was conducted by actuating the soft module such that the plane angle ϕ was constant during the whole characterisation. A single chamber was actuated with a pressure

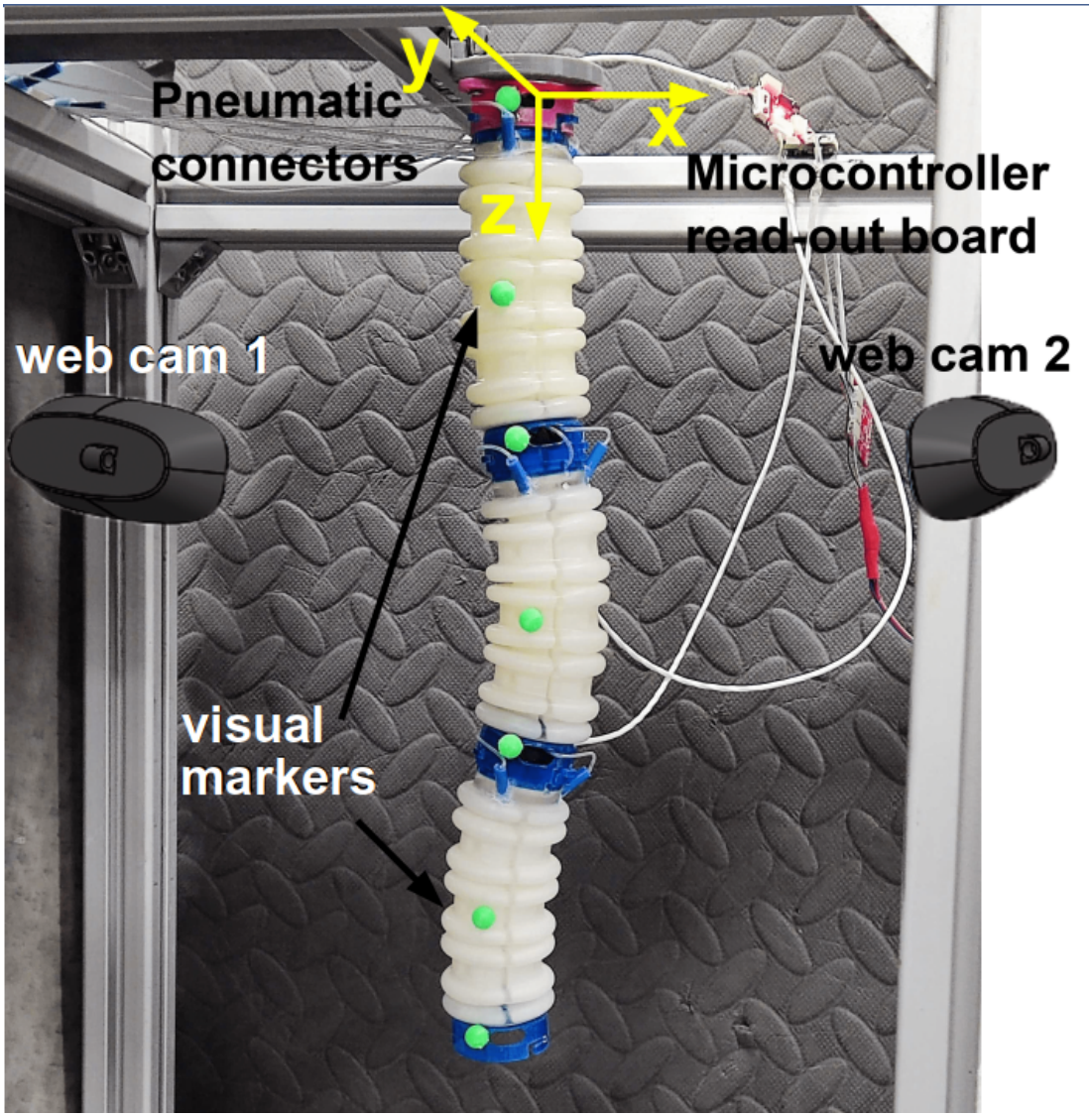


Figure 4.4: Front view of the experimental setup. Two cameras are employed to obtain the positions of the green visual markers placed on the soft robotic arm. Using the Algorithm 4.1, the positions of the markers could be converted into kinematic parameters of the PCC model which describe the spatial configuration of the soft arm

ranging in (0, 15) kPa with increments of 0.5 KPa. The bending angle of the module and the corresponding actuation pressure were recorded when the module reached its steady states. At the end of the procedure, the module was fully deflated. This experiment was repeated 5 times to test the repeatability of the motion. Due to the axisymmetric layout of the chambers, there were only two different actuation patterns to cause the module to bend as shown in Fig. 4.6, namely pressurising one chamber and pressurising two adjacent chambers. We simultaneously actuated two chambers within the same pressure range with increments of 0.5 kPa.

On the right of Fig. 4.6, we illustrate how the kinematic parameters of our soft module vary as its actuation pressure gradually increases to 15 kPa. As the actuation pressure rises, both

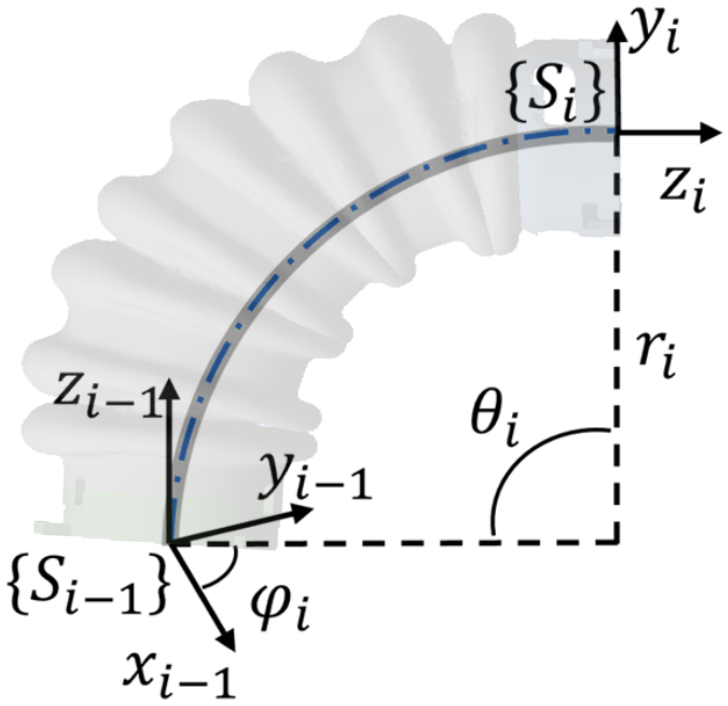


Figure 4.5: Constant curvature model of i-th module. The kinematics of the soft module is described by parameters r_i, θ_i, ϕ_i

actuation patterns lead to an increase in the bending angle of the module. Starting from 0 degree, the module eventually bends to approximately 45 degree under 15 kPa regardless of the actuation pattern. However, the relationship between the actuation pressure and the bending angle can be considered as linear when the single chamber was actuated with a pressure ranging in (3, 12) kPa, while this relationship was nonlinear for two chambers inflation. He et al. [2021] suggested that increasing the number of the embedded internal constraint structures could mitigate the nonlinearity of the bending performance caused by the nonlinear nature of the soft materials. It is also worth of notice that, under constant curvature assumption, the product of the bending angle θ and r is equal to the arc length which is equivalent to the length of the module. When the bending angle is zero, the length of the arc radius is infinity while it rapidly drops to approximately 150 mm as the bending angle reaches 45 degree.

Algorithm 4.1 Marker positions to CC parameters

Input: Top marker coordinates **A**, Middle marker coordinates **B**, Bottom marker coordinates **C**

1: $\mathbf{n}=\frac{\mathbf{A}\times\mathbf{B}+\mathbf{C}\times\mathbf{A}+\mathbf{B}\times\mathbf{C}}{|\mathbf{A}\times\mathbf{B}+\mathbf{C}\times\mathbf{A}+\mathbf{B}\times\mathbf{C}|}$ ▷ Calculate the normal vector **n** to the plane

2: $\boldsymbol{u} = (\boldsymbol{C} - \boldsymbol{A}) \times \boldsymbol{n}$

3: $\boldsymbol{v} = \boldsymbol{n} \times \boldsymbol{u}$ ▷ Find mutual orthogonal directions

4: $\mathbf{R} = [\boldsymbol{u}\ \boldsymbol{v}]$ ▷ Construct a rotation matrix from 3 direction vectors

5: d = $\boldsymbol{n} \cdot \boldsymbol{A}$ ▷ Find the distance between plane $\boldsymbol{ABC}$ to the origin

6: $\boldsymbol{a} = \begin{pmatrix} a_x \\ a_y \end{pmatrix} = \mathbf{R}^\top \boldsymbol{A}$

7: $\boldsymbol{b} = \begin{pmatrix} b_x \\ b_y \end{pmatrix} = \mathbf{R}^\top \boldsymbol{B}$

8: $\boldsymbol{c} = \begin{pmatrix} c_x \\ c_y \end{pmatrix} = \mathbf{R}^\top \boldsymbol{C}$ ▷ Convert the 3D problem into 2D plane

9: $\begin{bmatrix} b_x - a_x & b_y - a_y \\ c_x - a_x & c_y - a_y \end{bmatrix} \begin{pmatrix} x \\ y \end{pmatrix} = \begin{pmatrix} \frac{(b_x^2+b_y^2)-(a_x^2+a_y^2)}{2} \\ \frac{(c_x^2+c_y^2)-(a_x^2+a_y^2)}{2} \end{pmatrix}$ ▷ Find arc centre point coordinates in 2D plane

10: $\boldsymbol{Q} = \boldsymbol{n}\, d + \mathbf{R} \begin{pmatrix} x \\ y \end{pmatrix}$ ▷ Find arc centre point coordinates in 3D space

11: $r = \|\boldsymbol{A} - \boldsymbol{Q}\|$ ▷ Calculate the radius r

12: $\theta = \cos^{-1}\left(\frac{(\boldsymbol{C}-\boldsymbol{Q})\cdot(\boldsymbol{A}-\boldsymbol{Q})}{\|\boldsymbol{C}-\boldsymbol{Q}\|\,\|\boldsymbol{A}-\boldsymbol{Q}\|}\right)$ ▷ Calculate the arc angle θ

13: $\phi = \cos^{-1}\left(\frac{\boldsymbol{n}\boldsymbol{n}_{\boldsymbol{xz}}}{|n||n_{xz}|}\right)$ ▷ Calculate ϕ, the angle between $\boldsymbol{ABC}$ plane and xz plane

Output: Arc radius r, Arc angle θ, Orientation angle ϕ

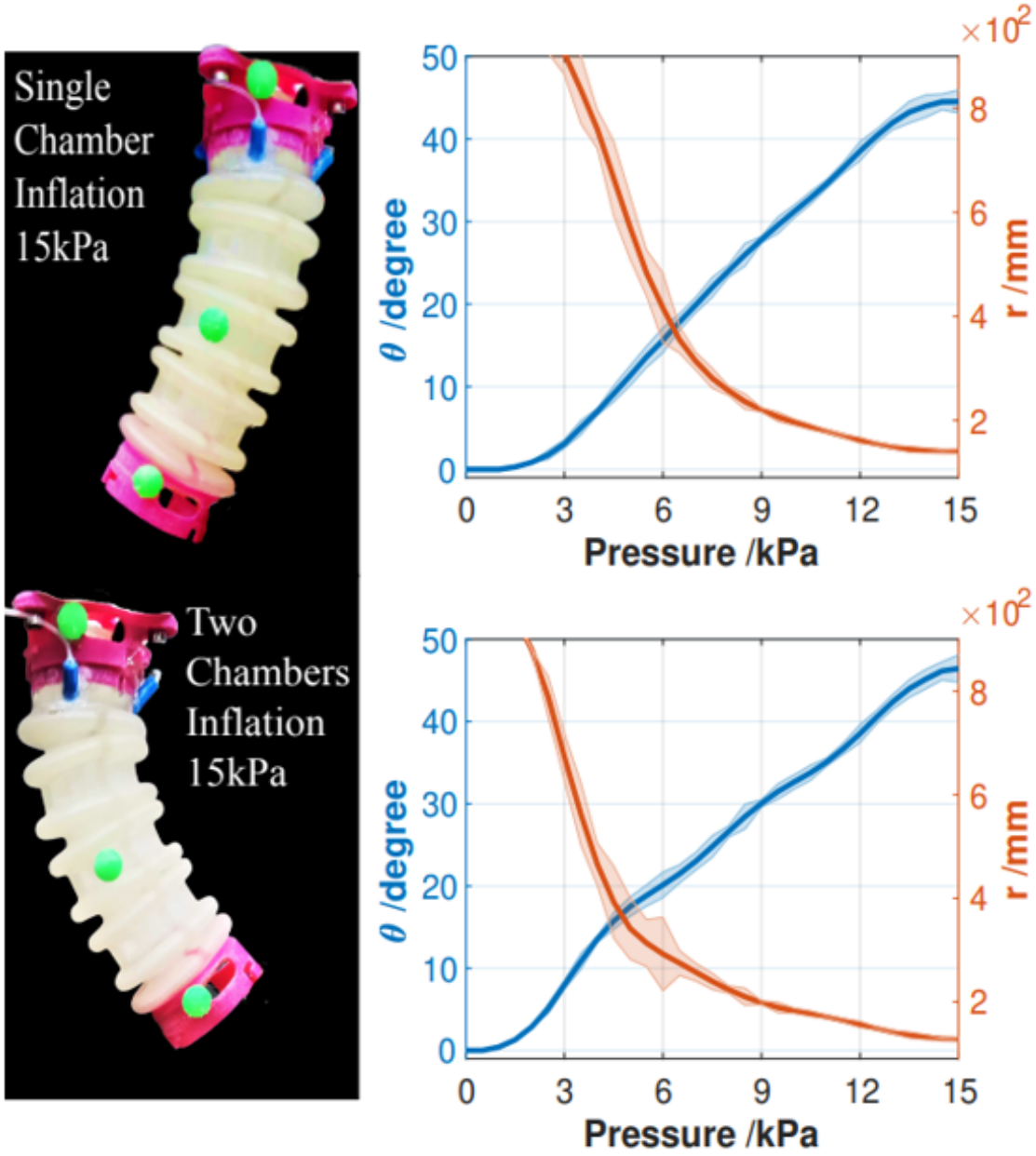


Figure 4.6: Module bending characterisation. The left subfigures show the bending motion of the module when one chamber is inflated (top) and two chambers are inflated to the same amount of pressure (bottom); The right subfigures illustrate the actuation pressure against the bending angle θ and arc radius r respectively when one (top) or two chambers (bottom) are inflated.

5

Proprioception of soft robotic arm using in-joint sensors

In this chapter, we explain how the spatial configuration of the multisegment soft robotic arm can be reconstructed using the in-joint sensor feedback in free space. We first look into the sensor responses ($\boldsymbol{P}$) when the soft module moves within its workspace while driven by air pressure and external forces to investigate how the movement of a single soft module affects the stress distribution over its top. Then we parameterise the spatial configuration of the three-segment soft robotic arm under piecewise constant curvature (PCC) assumption so the spatial configuration of the robot (β) can be predicted as the output of a k-NN regressor. We explain how the data was collected to train a k-NN regressor which maps the sensor responses to the spatial configuration of the whole arm. Lastly, we demonstrate that the spatial configuration of the whole arm could be reconstructed using the embedded sensor responses and the trained k-NN regressor as the Fig. 5.1 indicates.

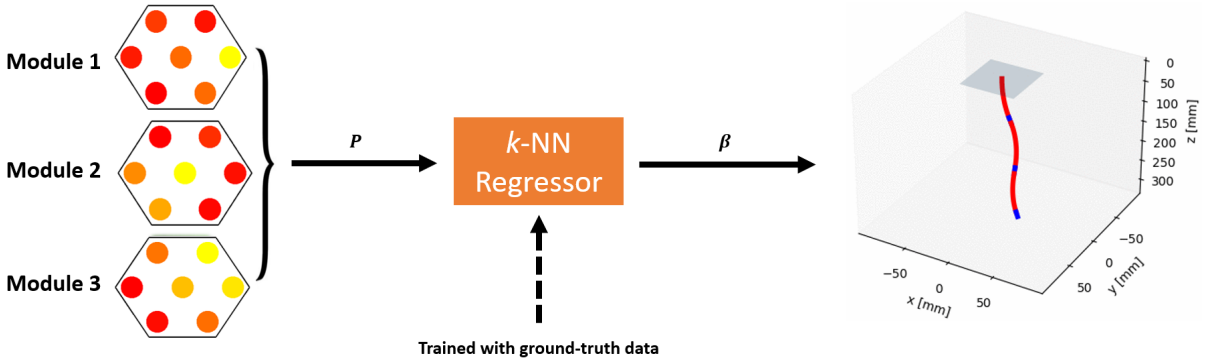


Figure 5.1: k-NN regressor mapping sensor responses $\boldsymbol{P}$ to kinematic parameters β. Under PCC assumption, the shape information of the soft arm can be reconstructed with the knowledge of β (Brighter taxels indicate higher sensor responses)

5.1 Stress distribution and soft robot motion

According to [Scimeca et al. [2019]], the posture of a tendon-driven soft robot is related to the stress distribution over its top. It can be observed that the magnitude and area of the stress

distribution vary at specific locations due to the pulling force exerted by the tendon. This shows the stress distribution is indicative of the posture of the soft body.

Since our soft robotic arm was pneumatically driven, we repeated the experiment described in Section 4.3 to investigate the relationship between the actuation pressure and the top plane stress distribution in two different actuation patterns. $p_1, ..., p_7$ represent the sensor responses captured by the 7 taxels. The spacious layout of the taxels is shown in Fig. 5.2. As can be observed in Fig. 5.2, all taxels respond differently to the rise in the magnitude of the actuation pressure. Scimeca et al. [2019] have demonstrated that the change in soft robot posture can cause an increase in the top plane stress distribution captured by the sensing unit. In our cases, the sensor responses drop due to the combined effect of the change in robot posture and the actuation pressure - it is difficult to find an analytical model to describe the relationship between the sensor responses and the soft robot posture.

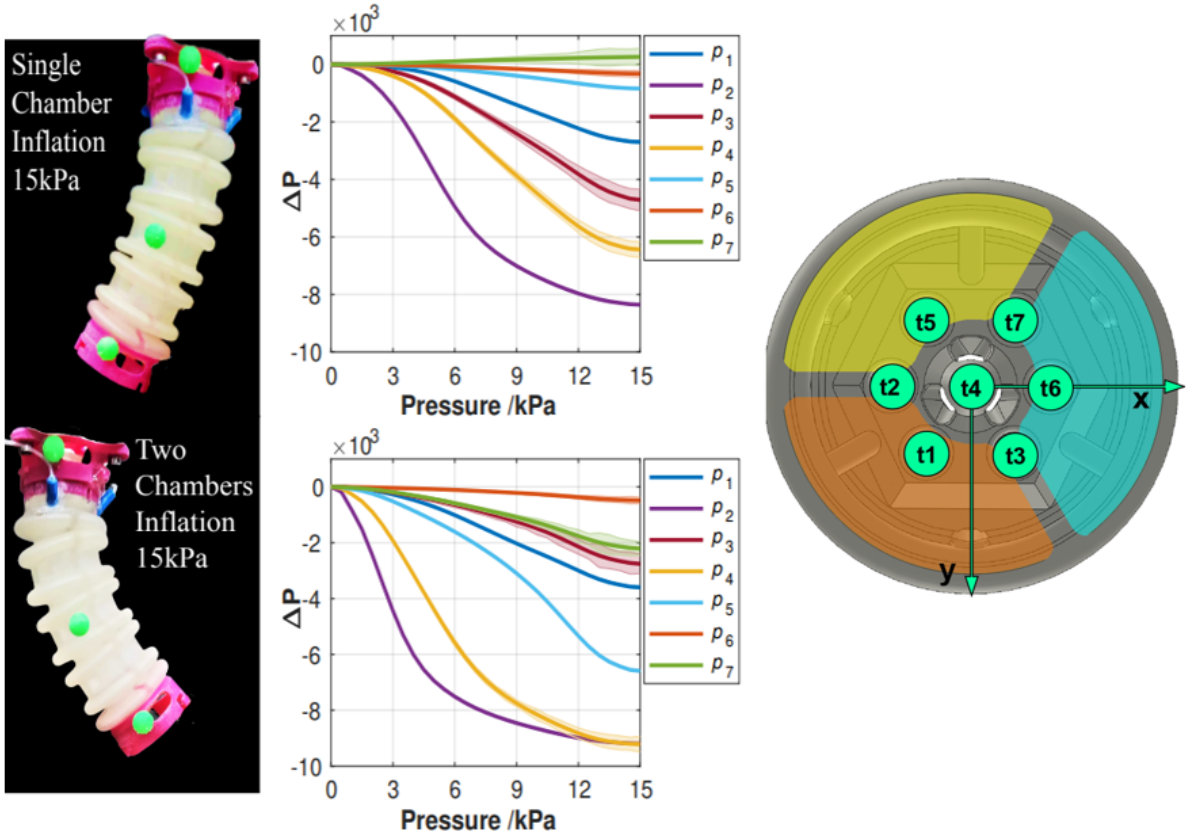


Figure 5.2: Characterisation of the top plane stress distribution. The plots show the relationship between the actuation pressure and the stress distribution measured by the sensing array in two actuation patterns: Single chamber inflation (Top) and two chambers inflation (Down). Spacious layout of the taxels on the sensor is provided.

To further characterise the stress distribution over the top of the soft module, we replicated

the experiment conducted in [Scimeca et al. [2019]] whose results can be found in Fig. 5.3.

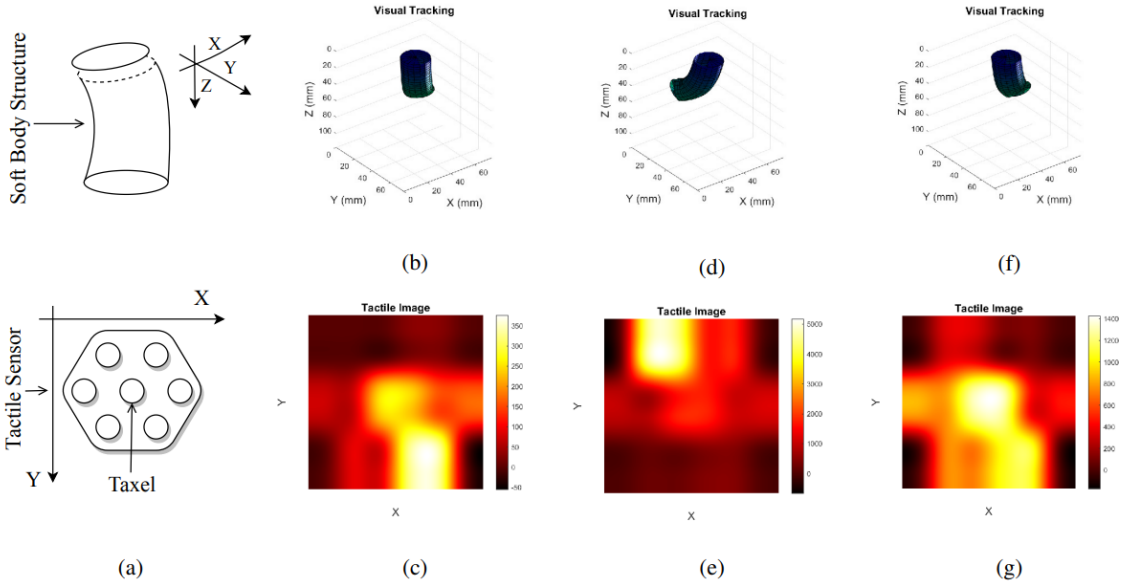


Figure 5.3: Stress distribution over the top plane induced by the change in the posture of the soft robot. (a) represents the coordinate system for the row. Subfigures (b), (d) and (f) show the visually tracked soft robot posture and subfigures (c), (e) and (g) shows the sensor responses where yellow indicates higher sensed pressure [Scimeca et al. [2019]]

Instead of investigating the stress distribution at few specific positions, we intended to survey the entire workspace of the soft robot and investigate how every single taxel responds. Due to the differences in design and actuation method, we recorded the responses from all taxels when the tip of the soft module moves within its workspace by 1) commanding pressures to the chambers and 2) when subjected to external forces (as in [Scimeca et al. [2019]]). Fig. 5.4 illustrates the experimental setup.

The tip of the module moves in a workspace of radius 25 mm in two different ways: 1) using the pneumatic actuation system to command 470 random pressure values in the interval (0, 15) KPa; 2) by placing an obstacle in contact with the tip of the module in 470 arbitrary locations to resample the workspace (see Fig. 5.4). The taxel responses were collected when the module was in a steady-state condition. The results of the experiment are plotted in Fig. 5.6 and Fig. 5.5 respectively.

In Fig. 5.3, a tendon-driven soft robot shows 3 different postures (b), (d) and (f), due to the pulling force exerted by the tendon. The corresponding taxel responses are plotted in subfigures (c), (e) and (g) and the increasing brightness indicates higher responses. It is evident that as the soft robot bends, the taxels sense higher pressure along the bending direction. As can be seen in

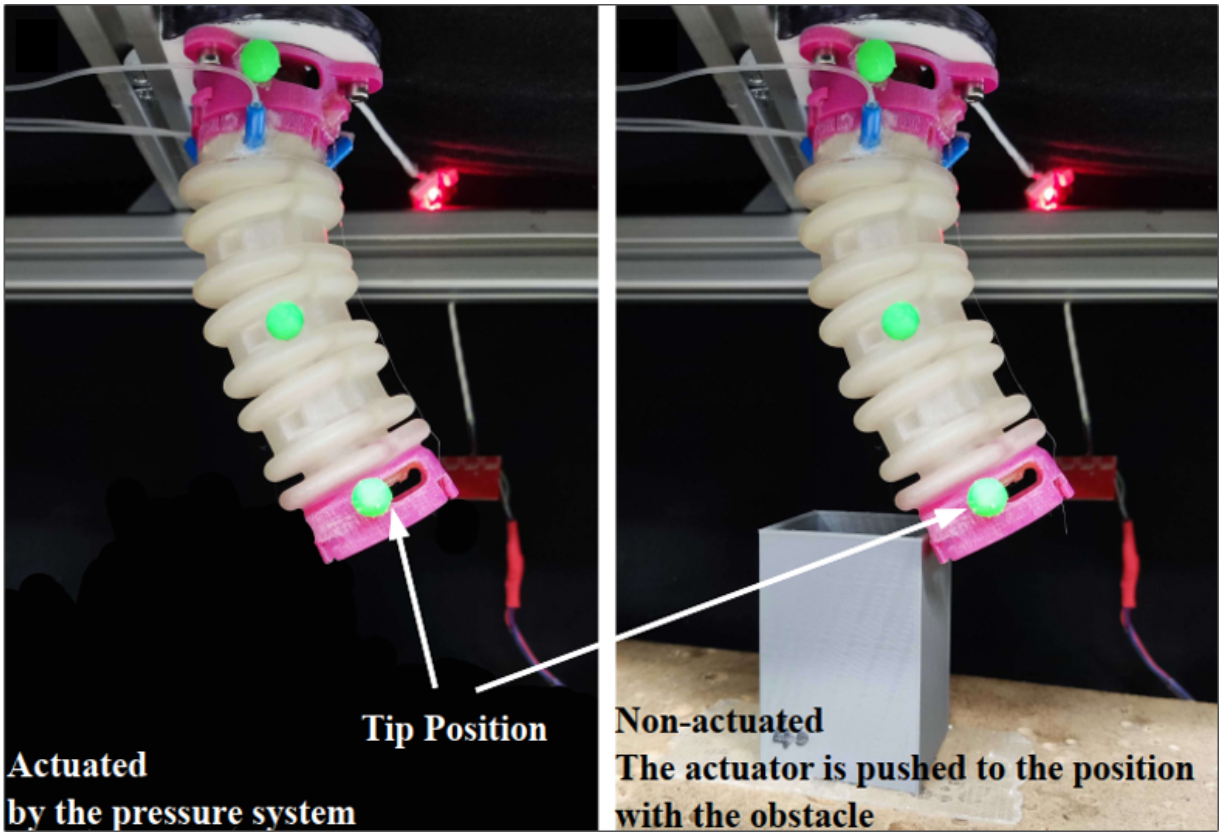


Figure 5.4: The experimental setup for characterising how the stress distribution on the top of the module changes in regard to the tip position. We compared the sensor responses when the module was pneumatically actuated and subjected to an external contact. On the left, the module is actuated by the pressure system to allow the tip to be freely explored in the workspace (the circle with a diameter of 25 mm in the XY-plane). On the right, the module is pushed to the configuration to allow the tip position maintained in the same workspace. The module is not actuated by the internal pressure.

Fig. 5.5, when our soft module is subjected to external forces, the corresponding taxel responses show the same trend that they increase as the soft robot bends towards the directions of the taxels.

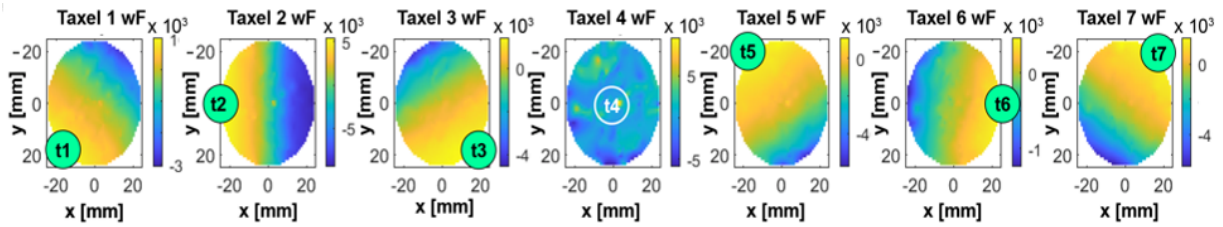


Figure 5.5: Taxel sensor responses at different locations in the XY-plane **when the robot tip being pushed by an external force**. $t_1, ..., t_7$ indicate the relative positions of the taxels.

When the soft module bends due to pneumatic actuation, the sensor responses are affected by both the inflation of the chambers and the movement of the module. Therefore, we also investigated how the taxel responses vary when the soft module was actuated by a pneumatic system and reported the results in Fig. 5.6. Although the patterns of taxel responses seem more

complicated than the responses reported in Fig. 5.5, it is observable that the corresponding taxel responses become stronger when the actuated module bends towards the taxels. This implies that the taxel responses are indicative of the posture of the pneumatically-driven soft module.

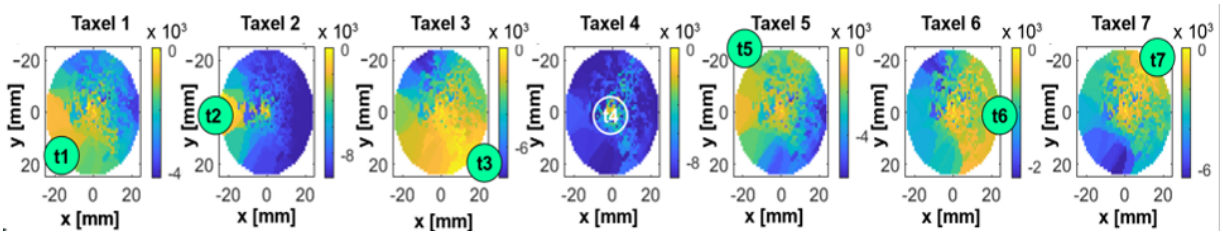


Figure 5.6: Taxel sensor responses at different locations in the XY-plane **when the robot was actuated**. $t_1, ..., t_7$ indicate the relative positions of the taxels.

5.2 Piecewise constant curvature kinematic model

Three modules are interconnected by the joint connectors forming a kinematic chain as shown in Fig. 5.7. The spatial configuration the i-th module is approximated with a CC model (see Fig. 4.5) and hence each of them is defined by three kinematic parameters r_i, θ_i and ϕ_i [Webster III and Jones [2010]], as previously discussed in Chapter 4.

Fig. 5.7 illustrates the kinematic model of the three-segment soft robotic arm, taking into account the rigid joints, where $\{S_0\}$ is the base frame and $\{S_i\}$ defines the frame at the end of rigid connector fixed to the tip of the $i-$th arc. The position and orientation of the tip of the $i-$th segment with respect to its parent frame $\{S_{i-1}\}$ can be expressed with the following transformation matrix:

$$T^i_{i-1}(r_i, \theta_i, \phi_i) = \bar{T}^i_{i-1}(r_i, \theta_i, \phi_i) \begin{bmatrix} I_3 & \mathbf{d} \\ \mathbf{0} & 1 \end{bmatrix} \tag{5.1}$$

where I_3 is the 3×3 identity matrix and $\mathbf{d} = [0, 0, d]^\intercal$, with $d \in \Re$ representing the constant length of the rigid connection. The transformation matrix $\bar{T}^i_{i-1}(r_i, \theta_i, \phi_i)$ based on the CC approximation has the following structure:

$$\bar{T}^i_{i-1}(r_i, \theta_i, \phi_i) = \begin{bmatrix} R^i_{i-1}(\theta_i, \phi_i) & \mathbf{p}^i_{i-1}(r_i, \theta_i, \phi_i) \\ \mathbf{0} & 1 \end{bmatrix} \tag{5.2}$$

where $R^i_{i-1}(\theta_i, \phi_i) \in \Re^{3\times3}$ and $\mathbf{p}^i_{i-1}(r_i, \theta_i, \phi_i) \in \Re^{3\times1}$ correspond to the rotation matrix and the translation vector defined in Webster III and Jones [2010]:

$$R^i_{i-1}(\theta_i, \phi_i) = \begin{bmatrix} \mathrm{c}^2_{\phi_i}(\mathrm{c}_{\theta_i} - 1) + 1 & \mathrm{s}_{\phi_i}\mathrm{c}_{\phi_i}(\mathrm{c}_{\theta_i} - 1) & \mathrm{c}_{\phi_i}\,\mathrm{s}_{\theta_i} \\ \mathrm{s}_{\phi_i}\mathrm{c}_{\phi_i}(\mathrm{c}_{\theta_i} - 1) & \mathrm{c}^2_{\phi_i}(1 - \mathrm{c}_{\theta_i}) + \mathrm{c}_{\theta_i} & \mathrm{s}_{\phi_i}\,\mathrm{s}_{\theta_i} \\ -\mathrm{c}_{\phi_i}\,\mathrm{s}_{\theta_i} & -\mathrm{s}_{\phi_i}\,\mathrm{s}_{\theta_i} & \mathrm{c}_{\theta_i} \end{bmatrix} \tag{5.3}$$

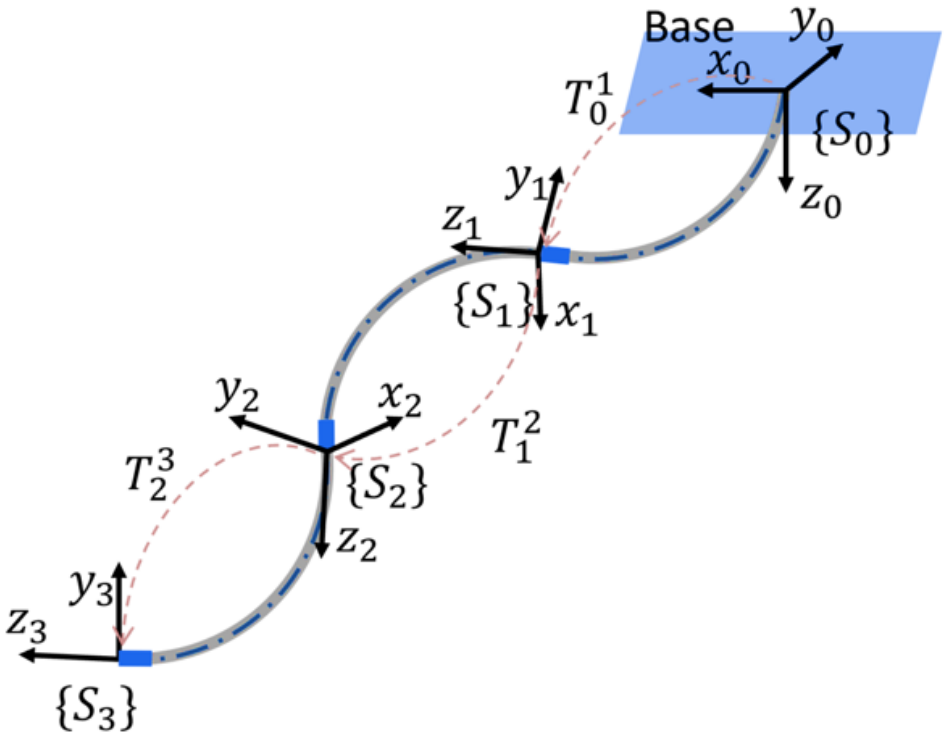


Figure 5.7: PCC kinematic model of the three-segment soft robotic arm. It consists of three interconnected CC model described in Fig. 4.5. T is the transformation matrix between the base of a curve and its tip

and

$$\mathbf{p}_{i-1}^{i}\left(r_i, \theta_i, \phi_i\right) = \mathrm{r_i}\left[\mathrm{c}_{\phi_i}\left(1-\mathrm{c}_{\theta_i}\right) \quad \mathrm{s}_{\phi_i}\left(1-\mathrm{c}_{\theta_i}\right) \quad \mathrm{s}_{\theta_i}\right]^{\mathrm{T}} \tag{5.4}$$

where c_{θ_i}, s_{θ_i}, c_{ϕ_i}, s_{ϕ_i} are $\cos\left(\theta_i\right), \sin\left(\theta_i\right), \cos\left(\phi_i\right), \sin\left(\phi_i\right)$ respectively.

5.3 k-NN regressor

According to Section 5.2, the spatial configuration of the three-segment soft robotic arm is represented by the following vector of parameters:

$$\boldsymbol{\beta} = [r_1, \theta_1, \phi_1, r_2, \theta_2, \phi_2, r_3, \theta_3, \phi_3]^{\intercal} \tag{5.5}$$

At a given time instant, the sensors provide a set of measurements $\mathrm{P} = \{p_1, p_2, \ldots, p_N\}$ where N is the number of taxels. As Fig. 5.1 shows, our goal is to define a model $M(\mathrm{P}) \rightarrow \boldsymbol{\beta}$ mapping the raw taxel responses obtained for a given soft robotic arm configuration with the kinematic parameters describing it. Due to the complexity of modelling the relationship between the soft robotic arm configuration and the stress distribution sensed by the sensing arrays, we considered to employ a data-driven approach to learn this mapping. Among the possible machine learning based models, in this paper, the use of a k-NN regressor has been considered for this task. The rationale behind this choice is given in [Kim et al. [2021]], where the current applications of

machine learning in the field of soft robotics are reviewed. In the review, several machine learning techniques were compared such as Support vector machines (SVMs), decision trees, Gaussian processes, linear models, Artificial neural networks (ANN) and k-nearest neighbors (k-NN) and employed them as regression models to estimate the deformations of soft robots (bending and twisting angles). They concluded that k-NN provides the best overall performance with low average error and model bias. Furthermore, compared to neural networks who demand large training data and complex hyperparameter tuning, k-nearest neighbors regression is able to achieve sufficient accuracy with relatively small training data.

The dataset used to train the k-NN model consisted of H pairs of samples P_h and $\boldsymbol{\beta}_h$ corresponding to the sensor readings and the configuration parameters related to a specific robot posture respectively. The output of the k-NN regressor corresponds to $\hat{\boldsymbol{\beta}}_h$, i.e. the estimated kinematic parameters, is defined as follows:

$$\hat{\boldsymbol{\beta}} = [\hat{r}_1, \hat{\theta}_1, \hat{\phi}_1, \hat{r}_2, \hat{\theta}_2, \hat{\phi}_2, \hat{r}_3, \hat{\theta}_3, \hat{\phi}_3]^\intercal \tag{5.6}$$

To train and evaluate the k-NN regressor we collected a dataset of pairs $\{\mathrm{P}_h, \boldsymbol{\beta}_h\}$ corresponding to the 21 readings and the 9 kinematic parameters associated to the h-th soft robotic arm posture at 20 Hz.

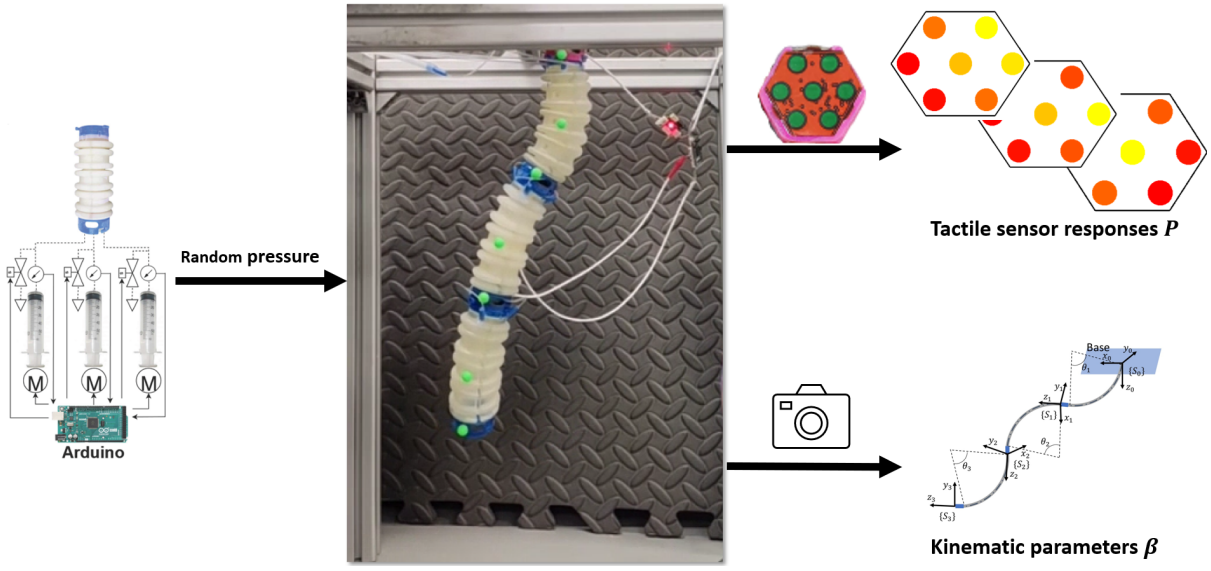


Figure 5.8: Schematic of the experimental setup for data collection. Three sets of pneumatic actuation system were employed to deliver random pressure input to all chambers of the soft arm to drive the arm to arbitrary positions. Meanwhile, our CySkin sensors and motion capture system captured the corresponding readings P and kinematic parameters β who were then used to train the model after data collection

The soft arm was actuated to generate $H = 908$ unique spatial configurations. As shown in Fig. 5.8, following a Random Search approach, the soft arm postures were generated by

assigning a set of desired pressures to the 9 chambers arbitrarily selected from an interval ranging from (0, 15) kPa with increments of 0.5 KPa. When the soft arm reached the steady-state, the sensor feedback P_h was collected, together with the positions of green markers placed along the soft robot arm. After the data collection, the kinematic parameters $\boldsymbol{\beta}_h$ describing the configuration of each segment under CC assumption, were computed from the marker positions as described in Algorithm 4.1.

5.3.1 Model training

Scikit-learn, an open source machine learning library was employed to implement k-NN in order to derive the mapping between the CySkin sensor responses and the kinematic parameters at steady-state and evaluate the performance. The dataset $\{\mathrm{P}, \boldsymbol{\beta}\}$ was split in train (80%) and test (20%) sets. The model was trained using the Euclidean distance between $\hat{\boldsymbol{\beta}}$ and $\boldsymbol{\beta}$ as distance metric (angles have been converted into unitary vectors when computing the distance). Furthermore, since the k-NN regressor requires a proper choice of the parameter k avoiding to overfit or underfit the data, a k-fold cross-validation [Kohavi et al. [1995]] has been performed on the training data, leading to the choice of $k = 4$, minimizing the distance function (see Equation 5.7) on the validation folds.

The working principle of the k-NN algorithm consist of finding similarities on the data based on a distance metric. We consider a distance function defined as:

$$\mathrm{J} = \frac{1}{2}\mathbf{e}^{\intercal}\mathbf{e} \tag{5.7}$$

where $\mathbf{e} = [e_r, e_\theta, e_\phi] \in \Re^3$ is a vector, containing the error among the predicted and ground-truth kinematic parameters describing the soft robotic arm posture. The specific error terms are defines as:

$$e_r = \sqrt{\sum_{i=1}^{3} \left(\hat{r}_i - r_i\right)^2} \tag{5.8}$$

$$e_\theta = \sqrt{\sum_{i=1}^{3} \left(\sin^{-1}\left(\sin\hat{\theta}_i \cos\theta_i - \cos\hat{\theta}_i \sin\theta_i\right)\right)^2} \tag{5.9}$$

$$e_\phi = \sqrt{\sum_{i=1}^{3} \left(\sin^{-1}\left(\sin\hat{\phi}_i \cos\phi_i - \cos\hat{\phi}_i \sin\phi_i\right)\right)^2} \tag{5.10}$$

To test the convergence of our training, we provided between 10% to 100% of training dataset to the k-NN in increments of 10%. Fig. 5.9 shows how the average position estimation

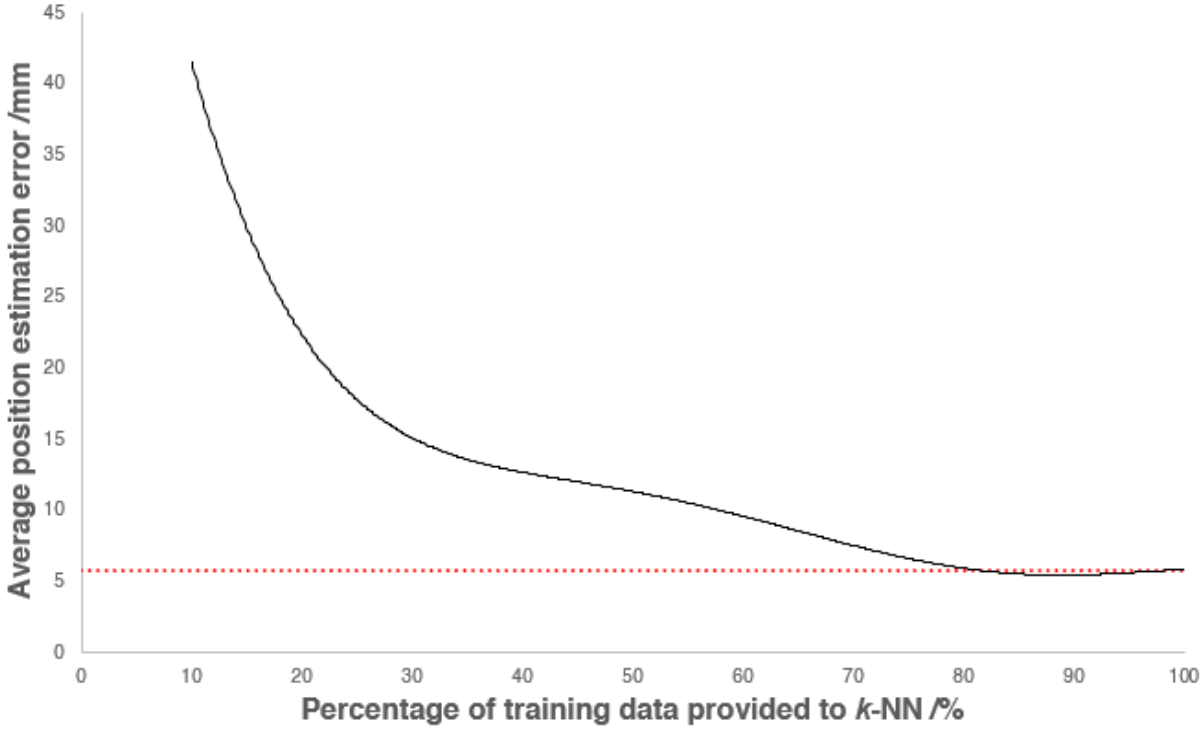


Figure 5.9: k-NN training convergence

error falls as the amount of training dataset increases. The error drops dramatically as the percentage of training data rises from 10% to 30%. Then the error decreases steadily as the percentage of training data increases from 30% to 80%. Eventually, the mean estimation error no longer decreases as more training data is provided and we can conclude that the k-NN estimator has converged.

5.4 Experimental validation

To evaluate the performance of the trained k-NN regressor, we calculated the error between the kinematic parameters β (computed using the Algorithm 4.1) and the estimated parameters $\hat{\beta}$. Table 5.1 shows the result of the k-NN regressor applied on the test data, reporting for each one of the three modules (from top to bottom), the mean estimation errors $\bar{e}_r$, $\bar{e}_\theta$ and $\bar{e}_\phi$ for the three kinematic parameters.

Table 5.1: Mean estimation error for parameters describing the kinematics of each module

	$\bar{e}_r$ (mm)	$\bar{e}_\theta$ (rad)	$\bar{e}_\phi$ (rad)
Module 1	53.86	0.028	0.096
Module 2	38.90	0.033	0.069
Module 3	45.95	0.038	0.051

Module 1 refers to the module that is the closest to the fixed end while Module 3 refers

to the module that is the closest to the free end. Although the mean errors in the arc radius for all three modules are large, especially for the Module 1 (over 5 cm), they do not directly translate to the actual distance error in the 3D space. As shown in Fig. 4.6, the value of arc radius is infinity when the soft module is at its rest and then drop significantly to approximately 150 mm as the module bends to 45 degree. The errors in the bending angles across all three modules are about 0.03 rads which is 1.72 degree. Since the arc length is equal to the product of the bending angle and the arc radius, the small errors in the bending angles indicate that the estimation is accurate. Lastly, the highest error in the orientation angle can be observed in Module 1 and it is small compared to its motion range.

Overall, the trained k-NN regressor was able to give a accurate prediction on the values of the kinematic parameters which can reconstruct the posture of the three-segment soft robotic arm. Furthermore, $\hat{\boldsymbol{\beta}}$ can be substituted on the equations describing the forward kinematic (see Section 5.2) to obtain the Cartesian coordinates of the tip of the soft arm with respect to the base frame. The parameters $\hat{\boldsymbol{\beta}}$ related to the results presented in Table 5.1, allowed to estimate the position of the tip with a mean error $\bar{e}_x = 5.64$ mm and with a low standard deviation $\sigma_x = 1.91$ mm. The error was computed on the test set as the Euclidean distance between the predicted and the ground-truth tip position captured by the motion capture system as shown in Fig. 4.4.

Since it is impractical to present the shape reconstruction of every possible posture of the soft robotic arm, we arbitrarily picked three postures and provide the full results of the reconstruction of the shape of the actuated soft robotic arm including the corresponding kinematic parameters and the tip errors (see Fig. 5.10). Using the motion capture system, the ground-truth kinematic parameters $\boldsymbol{\beta}$ was computed from the captured marker positions using Algorithm 4.1. On the other hand, having the sensor responses $\boldsymbol{P}$ as the input, the trained k-NN regressor outputs the estimated parameters $\hat{\boldsymbol{\beta}}$ (see Fig. 5.1). With the PCC model of the whole arm (Equation. 5.1), the spatial configuration of the soft arm can be reconstructed given the kinematic parameters $\boldsymbol{\beta}$ and $\hat{\boldsymbol{\beta}}$. Fig. 5.10(Top) shows the pictures of the soft arm and the bottom row show the corresponding plots of the ground-truth and predicted configurations. In the plots, the black and red-blue lines represent the ground-truth and estimated posture of the soft arm respectively. Close views of the tip positions are provided with a double direction purple arrow indicating the prediction error. The corresponding kinematic parameters $\boldsymbol{\beta}$ and $\hat{\boldsymbol{\beta}}$ are listed in the Table 5.2:

As previously discussed, it is noteworthy that the large errors in the arc radius do not imply inaccurate predictions. In example (a), the error in the arc radius of Module 3 was over 9 cm. Similarly, the error in radius of Module 1 in example (b) was also higher than 9 cm. However,

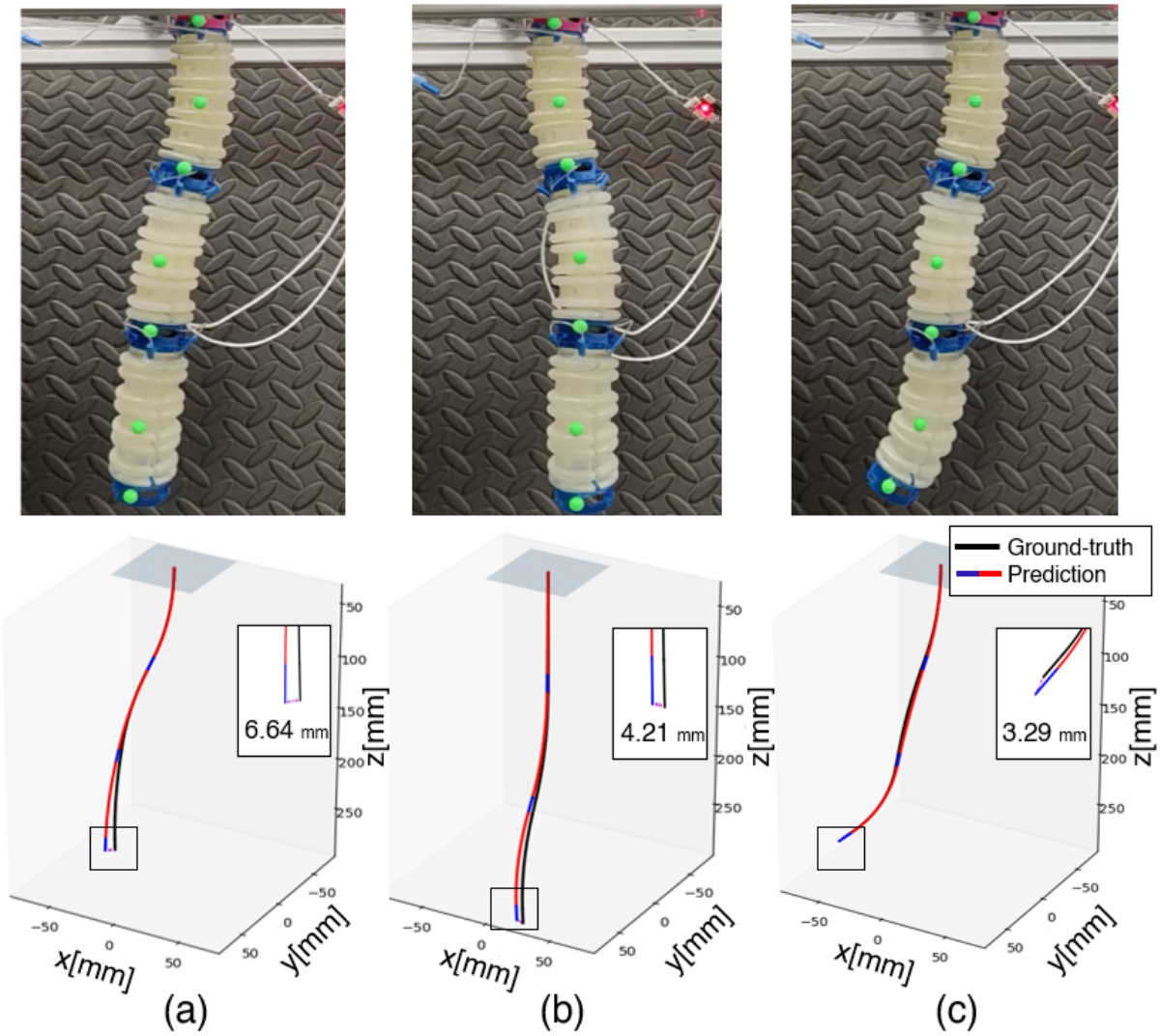


Figure 5.10: Examples of the posture reconstruction obtained using the k-NN regressor. With the ground-truth kinematic parameters β and estimated kinematic parameters $\hat{\beta}$, the real and estimated spatial configuration can be reconstructed and plotted. The black curve represents the ground-truth while the blue-red curve represents the estimation and the blue colour indicates the rigid parts. The errors in estimating the tip positions are magnified and showed on each subfigure

the final tip errors in both examples were low and they presented good estimations of the overall shape of the soft robotic arm as shown in Fig. 5.10.

Table 5.2: Real and estimated kinematic parameters for the three examples in Fig. 5.10

		Example (a)		Example (b)		Example (c)	
		Real	Estimated	Real	Estimated	Real	Estimated
Module 1	r (mm)	248.29	269.15	507.65	416.19	345.65	397.49
	θ (rads)	0.380	0.343	0.189	0.211	0.276	0.239
	ϕ (rads)	1.830	1.894	0.786	0.736	1.729	1.816
Module 2	r (mm)	458.12	398.47	254.16	265.31	498.68	443.98
	θ (rads)	0.203	0.226	0.354	0.368	0.187	0.212
	ϕ (rads)	4.485	4.557	3.156	3.097	4.626	4.673
Module 3	r (mm)	601.57	697.14	289.51	261.76	145.73	151.25
	θ (rads)	0.151	0.125	0.311	0.344	0.621	0.603
	ϕ (rads)	5.026	5.073	5.589	5.514	2.351	2.384
Tip error (mm)		6.64		4.21		3.29	

6
Conclusions

In this Chapter, we summarise the main research outcomes of the project and outline the limitations of the study. To recap, this thesis proposed a novel design of a 3D printable soft robotic arm that is capable of omnidirectional motion in the 3D space and retrieving its spatial configurations in the free space.

With the help of CAD software, we designed several soft pneumatic actuators with rigid joints that can be interconnected as modules to form a multisegment soft robotic arm. Due to its geometrical complexity, we chose to fabricate the modules using 3D printing technology. As soft module characterisation results show, the proposed design possesses good repeatability and is able to bend to 45 degree at 15 kPa pressure.

Sensing arrays are placed at the joint of the modules to measure the stress distribution over its top. Compared to embedding soft and stretchable sensors along the deformed body of the soft robot, the integration of the tactile sensors at the joint does not change the mechanical properties of the robot or interfere with the robot motion. The sensors also experience less relative movement with respect to the soft bodies compared to soft and flexible strain sensors, with a potential of an increased lifetime. Moreover, we experimentally showed that the relation between the tactile sensor responses and the spatial configuration of the robot can be learned by performing a k-NN regression.

With the learned mapping, we demonstrated that the spatial configuration can be estimated with the tactile sensor responses. We provided the errors in estimating the kinematic parameters which represent the spatial configuration of the whole arm under PCC assumption. We further evaluated the overall success of the shape reconstruction by comparing the differences in the predicted and actual tip positions and concluded that we have achieved proprioception for our multisegment soft robotic arm without external visual feedback.

Additionally, in order to conduct the experiments, a motion capture system was used to monitor the 3D motions of the soft robotic arm and a pneumatic actuation system that supplies desired amount of air pressure to the 9 chambers of the soft arm. They might be useful for further studies.

In conclusion, we provided a novel solution to the problem of endowing modular soft robotic arms with proprioception.

6.1 Limitations

Because of the time limitation and the inaccessibility to the high-priced hardware devices, the width of this project scope is limited and the performance of our system could be improved.

In order to capture the ground-truth 3D shape information, we used a motion capture system with 2 high resolution webcams and multiple coloured markers. In this field, a common option is to use commercially available motion capture system such as OptiTrack and Vicon [Satheeshbabu et al. [2020]; Truby et al. [2018]] which are able to capture the 3D motion data with low error at 100 Hz, while our system runs at 20 Hz.

The motion capture system ran at an adequate frequency as our soft robotic arm moved relatively slow. This is because of our actuation system cannot deliver sufficient amount of air pressure within a short time interval as it depends on the motor motions to drive the syringes. The low speed of our soft robotic arm constrained the size of our dataset and affected the performance of the trained regressor. A possible improvement is to use one high pressure air source together with multiple proportional valves which regulate the pressure within the chambers of the soft robotic arm to achieve high speed and potentially high force [Jiang et al. [2021]].

On the other hand, as introduced in the Chapter 2, there are several actuation methods for soft continuum actuators based on hydraulic actuation, shape memory alloy, variable length tendon and electro-active polymer[Lee et al. [2017]] while only pneumatically driven soft actuators are considered in this project. However, we believe our solution can be generalised to other multisegment soft robotic arms powered by different actuation methods as long as the stress distribution over the segment top is accessible.

References

Fady F Abayazid and Mazdak Ghajari. Material characterisation of additively manufactured elastomers at different strain rates and build orientations. *Additive Manufacturing*, 33:101160, 2020.

John Alexiou. 3 points in 3d space to find the center of an arc or circle. Mathematics Stack Exchange, 2019. URL https://math.stackexchange.com/q/3482172. URL:https://math.stackexchange.com/q/3482172 (version: 2019-12-19).

Faisal Aljaber, Ahmed Hassan, Ivan Vitanov, and Kaspar Althoefer. Curvature and contact sensing with optical waveguides for soft silicone pneumatic actuator. In *2022 IEEE 5th International Conference on Soft Robotics (RoboSoft)*, pages 859–864. IEEE, 2022.

Morteza Amjadi, Ki-Uk Kyung, Inkyu Park, and Metin Sitti. Stretchable, skin-mountable, and wearable strain sensors and their potential applications: a review. *Advanced Functional Materials*, 26(11): 1678–1698, 2016.

Yousef Bahramzadeh and Mohsen Shahinpoor. A review of ionic polymeric soft actuators and sensors. *Soft Robotics*, 1(1):38–52, 2014.

Roman Balak and Yi Chen Mazumdar. Multi-modal pneumatic actuator for twisting, extension, and bending. In *2020 IEEE/RSJ International Conference on Intelligent Robots and Systems (IROS)*, pages 8673–8679. IEEE, 2020.

A Burr and J Cheatham. Mechanical design and analysis, section 5.2, 1995.

Jean-Baptiste Chossat, Yong-Lae Park, Robert J Wood, and Vincent Duchaine. A soft strain sensor based on ionic and metal liquids. *Ieee sensors journal*, 13(9):3405–3414, 2013.

Matteo Cianchetti, Federico Renda, Alessia Licofonte, and Cecilia Laschi. Sensorization of continuum soft robots for reconstructing their spatial configuration. In *2012 4th IEEE RAS & EMBS International Conference on Biomedical Robotics and Biomechatronics (BioRob)*, pages 634–639. IEEE, 2012.

CySkin, 2022. URL https://www.cyskin.com/.

Abu Bakar Dawood, Hareesh Godaba, and Kaspar Althoefer. Modelling of a soft sensor for exteroception and proprioception in a pneumatically actuated soft robot. In *Annual Conference Towards Autonomous Robotic Systems*, pages 99–110. Springer, 2019.

Cosimo Della Santina, Robert K Katzschmann, Antonio Bicchi, and Daniela Rus. Model-based dynamic feedback control of a planar soft robot: trajectory tracking and interaction with the environment. *The International Journal of Robotics Research*, 39(4):490–513, 2020a.

Cosimo Della Santina, Ryan Landon Truby, and Daniela Rus. Data–driven disturbance observers for estimating external forces on soft robots. *IEEE Robotics and Automation Letters*, 5(4):5717–5724, 2020b.

Nazek El-Atab, Rishabh B Mishra, Fhad Al-Modaf, Lana Joharji, Aljohara A Alsharif, Haneen Alamoudi, Marlon Diaz, Nadeem Qaiser, and Muhammad Mustafa Hussain. Soft actuators for soft robotic applications: a review. *Advanced Intelligent Systems*, 2(10):2000128, 2020.

Nicholas Farrow and Nikolaus Correll. A soft pneumatic actuator that can sense grasp and touch. In *2015 IEEE/RSJ International Conference on Intelligent Robots and Systems (IROS)*, pages 2317–2323. IEEE, 2015.

Wyatt Felt, Khai Yi Chin, and C David Remy. Smart braid feedback for the closed-loop control of soft robotic systems. *Soft robotics*, 4(3):261–273, 2017.

Wyatt Felt, Maria J Telleria, Thomas F Allen, Gabriel Hein, Jonathan B Pompa, Kevin Albert, and C David Remy. An inductance-based sensing system for bellows-driven continuum joints in soft robots. *Autonomous robots*, 43(2):435–448, 2019.

Jan Fras, Jakub Glówka, and Kaspar Althoefer. Instant soft robot: A simple recipe for quick and easy manufacturing. In *2020 3rd IEEE International Conference on Soft Robotics (RoboSoft)*, pages 482–488. IEEE, 2020.

Hareesh Godaba, Ivan Vitanov, Faisal Aljaber, Ahmad Ataka, and Kaspar Althoefer. A bending sensor

insensitive to pressure: soft proprioception based on abraded optical fibres. In *2020 3rd IEEE International Conference on Soft Robotics (RoboSoft)*, pages 104–109. IEEE, 2020.

Bin He, Yanmin Zhou, Zhipeng Wang, Qigang Wang, Runjie Shen, and Shangqing Wu. A multi-layered touch-pressure sensing ionogel material suitable for sensing integrated actuations of soft robots. *Sensors and Actuators A: Physical*, 272:341–348, 2018.

Liang He, Xinyang Tan, Koichi Suzumori, and Thrishantha Nanayakkara. A method to 3d print a programmable continuum actuator with single material using internal constraint. *Sensors and Actuators A: Physical*, 324:112674, 2021.

Tim Helps and Jonathan Rossiter. Proprioceptive flexible fluidic actuators using conductive working fluids. *Soft robotics*, 5(2):175–189, 2018.

Bianca S Homberg, Robert K Katzschmann, Mehmet R Dogar, and Daniela Rus. Robust proprioceptive grasping with a soft robot hand. *Autonomous Robots*, 43(3):681–696, 2019.

Josie Hughes, Francesco Stella, Cosimo Della Santina, and Daniela Rus. Sensing soft robot shape using imus: An experimental investigation. In *International Symposium on Experimental Robotics*, pages 543–552. Springer, 2020.

Lorenzo Jamone, Lorenzo Natale, Giorgio Metta, and Giulio Sandini. Highly sensitive soft tactile sensors for an anthropomorphic robotic hand. *IEEE sensors Journal*, 15(8):4226–4233, 2015.

Hao Jiang, Zhanchi Wang, Yusong Jin, Xiaotong Chen, Peijin Li, Yinghao Gan, Sen Lin, and Xiaoping Chen. Hierarchical control of soft manipulators towards unstructured interactions. *The International Journal of Robotics Research*, 40(1):411–434, 2021.

Robert K Katzschmann, Cosimo Della Santina, Yasunori Toshimitsu, Antonio Bicchi, and Daniela Rus. Dynamic motion control of multi-segment soft robots using piecewise constant curvature matched with an augmented rigid body model. In *2019 2nd IEEE International Conference on Soft Robotics (RoboSoft)*, pages 454–461. IEEE, 2019a.

Robert K Katzschmann, Maxime Thieffry, Olivier Goury, Alexandre Kruszewski, Thierry-Marie Guerra, Christian Duriez, and Daniela Rus. Dynamically closed-loop controlled soft robotic arm using a reduced order finite element model with state observer. In *2019 2nd IEEE International Conference on Soft Robotics (RoboSoft)*, pages 717–724. IEEE, 2019b.

Daekyum Kim, Sang-Hun Kim, Taekyoung Kim, Brian Byunghyun Kang, Minhyuk Lee, Wookeun Park, Subyeong Ku, DongWook Kim, Junghan Kwon, Hochang Lee, et al. Review of machine learning methods in soft robotics. *Plos one*, 16(2):e0246102, 2021.

Min-gu Kim, Byeongyong Lee, Mochen Li, Suguru Noda, Choongsoon Kim, Jayoung Kim, Woo-Jin Song, Seung Woo Lee, and Oliver Brand. All-soft supercapacitors based on liquid metal electrodes with integrated functionalized carbon nanotubes. *ACS nano*, 14(5):5659–5667, 2020.

Ron Kohavi et al. A study of cross-validation and bootstrap for accuracy estimation and model selection. In *Ijcai*, volume 14, pages 1137–1145. Montreal, Canada, 1995.

Kenji Kure, Takefumi Kanda, Koichi Suzumori, and Shuichi Wakimoto. Flexible displacement sensor using injected conductive paste. *Sensors and Actuators A: Physical*, 143(2):272–278, 2008.

Nathan Lazarus and Sarah S Bedair. Bubble inductors: Pneumatic tuning of a stretchable inductor. *AIP Advances*, 8(5):056601, 2018.

Chiwon Lee, Myungjoon Kim, Yoon Jae Kim, Nhayoung Hong, Seungwan Ryu, H Jin Kim, and Sungwan Kim. Soft robot review. *International Journal of Control, Automation and Systems*, 15(1):3–15, 2017.

Chiara Lucarotti, Massimo Totaro, Ali Sadeghi, Barbara Mazzolai, and Lucia Beccai. Revealing bending and force in a soft body through a plant root inspired approach. *Scientific reports*, 5(1):1–10, 2015.

Ming Luo, Erik H Skorina, Weijia Tao, Fuchen Chen, Selim Ozel, Yinan Sun, and Cagdas D Onal. Toward modular soft robotics: Proprioceptive curvature sensing and sliding-mode control of soft bidirectional bending modules. *Soft robotics*, 4(2):117–125, 2017.

Zhonglei Ma, Ajing Wei, Yuntao Li, Liang Shao, Hongming Zhang, Xiaolian Xiang, Jingping Wang, Qinbo Ren, Songlei Kang, Diandian Dong, et al. Lightweight, flexible and highly sensitive segregated

microcellular nanocomposite piezoresistive sensors for human motion detection. *Composites Science and Technology*, 203:108571, 2021.

Geetika Maddirala, Thomas Searle, Xiao Wang, Gursel Alici, and Vitor Sencadas. Multifunctional skin-compliant wearable sensors for monitoring human condition applications. *Applied Materials Today*, 26: 101361, 2022.

Andrew D Marchese, Robert K Katzschmann, and Daniela Rus. Whole arm planning for a soft and highly compliant 2d robotic manipulator. In *2014 IEEE/RSJ International Conference on Intelligent Robots and Systems*, pages 554–560. IEEE, 2014.

John Morrow, Hee-Sup Shin, Calder Phillips-Grafflin, Sung-Hwan Jang, Jacob Torrey, Riley Larkins, Steven Dang, Yong-Lae Park, and Dmitry Berenson. Improving soft pneumatic actuator fingers through integration of soft sensors, position and force control, and rigid fingernails. In *2016 IEEE International Conference on Robotics and Automation (ICRA)*, pages 5024–5031. IEEE, 2016.

Joseph T Muth, Daniel M Vogt, Ryan L Truby, Yiğit Mengüç, David B Kolesky, Robert J Wood, and Jennifer A Lewis. Embedded 3d printing of strain sensors within highly stretchable elastomers. *Advanced materials*, 26(36):6307–6312, 2014.

Wenye Ouyang, Liang He, Alessandro Albini, and Perla Maiolino. A modular soft robotic arm with embedded tactile sensors for proprioception. In *2022 IEEE 5th International Conference on Soft Robotics (RoboSoft)*, pages 919–924. IEEE, 2022.

Selim Ozel, Nehir A Keskin, Darien Khea, and Cagdas D Onal. A precise embedded curvature sensor module for soft-bodied robots. *Sensors and Actuators A: Physical*, 236:349–356, 2015.

Jaeyoon Park, Insang You, Sangbaie Shin, and Unyong Jeong. Material approaches to stretchable strain sensors. *ChemPhysChem*, 16(6):1155–1163, 2015.

Yong-Lae Park, Bor-Rong Chen, and Robert J Wood. Design and fabrication of soft artificial skin using embedded microchannels and liquid conductors. *IEEE Sensors journal*, 12(8):2711–2718, 2012.

Brennan T Phillips, Kaitlyn P Becker, Shunichi Kurumaya, Kevin C Galloway, Griffin Whittredge, Daniel M Vogt, Clark B Teeple, Michelle H Rosen, Vincent A Pieribone, David F Gruber, et al. A dexterous, glove-based teleoperable low-power soft robotic arm for delicate deep-sea biological exploration. *Scientific reports*, 8(1):1–9, 2018.

Emanuele Riccardo Rosi, Maximilian Stölzle, Fabio Solari, and Cosimo Della Santina. Sensing soft robots' shape with cameras: an investigation on kinematics-aware slam. In *2022 IEEE 5th International Conference on Soft Robotics (RoboSoft)*, pages 795–801. IEEE, 2022.

Jonathan Rossiter and Helmut Hauser. Soft robotics—the next industrial revolution. *IEEE Robot. Autom. Mag*, 23(3):17–20, 2016.

Daniela Rus and Michael T Tolley. Design, fabrication and control of soft robots. *Nature*, 521(7553): 467–475, 2015.

Stefania Russo, Tommaso Ranzani, Hongbin Liu, Samia Nefti-Meziani, Kaspar Althoefer, and Arianna Menciassi. Soft and stretchable sensor using biocompatible electrodes and liquid for medical applications. *Soft robotics*, 2(4):146–154, 2015.

SM Hadi Sadati, Ali Shiva, Nicolas Herzig, Caleb D Rucker, Helmut Hauser, Ian D Walker, Christos Bergeles, Kaspar Althoefer, and Thrishantha Nanayakkara. Stiffness imaging with a continuum appendage: Real-time shape and tip force estimation from base load readings. *IEEE Robotics and Automation Letters*, 5(2):2824–2831, 2020.

Sina Sareh, Yohan Noh, Min Li, Tommaso Ranzani, Hongbin Liu, and Kaspar Althoefer. Macrobend optical sensing for pose measurement in soft robot arms. *Smart Materials and Structures*, 24(12): 125024, 2015.

Sreeshankar Satheeshbabu, Naveen K Uppalapati, Tianshi Fu, and Girish Krishnan. Continuous control of a soft continuum arm using deep reinforcement learning. In *2020 3rd IEEE International Conference on Soft Robotics (RoboSoft)*, pages 497–503. IEEE, 2020.

Rob BN Scharff, Guoxin Fang, Yingjun Tian, Jun Wu, Jo MP Geraedts, and Charlie CL Wang. Sensing and

reconstruction of 3-d deformation on pneumatic soft robots. *IEEE/ASME Transactions on Mechatronics*, 26(4):1877–1885, 2021.

François Schmitt, Olivier Piccin, Laurent Barbé, and Bernard Bayle. Soft robots manufacturing: A review. *Frontiers in Robotics and AI*, 5:84, 2018.

Alexander Schmitz, Perla Maiolino, Marco Maggiali, Lorenzo Natale, Giorgio Cannata, and Giorgio Metta. Methods and technologies for the implementation of large-scale robot tactile sensors. *IEEE Transactions on Robotics*, 27(3):389–400, 2011.

Luca Scimeca, Josie Hughes, Perla Maiolino, and Fumiya Iida. Model-free soft-structure reconstruction for proprioception using tactile arrays. *IEEE Robotics and Automation Letters*, 4(3):2479–2484, 2019.

Ethan B Secor, Alexander B Cook, Christopher E Tabor, and Mark C Hersam. Wiring up liquid metal: Stable and robust electrical contacts enabled by printable graphene inks. *Advanced Electronic Materials*, 4(1):1700483, 2018.

Gabor Soter, Andrew Conn, Helmut Hauser, and Jonathan Rossiter. Bodily aware soft robots: integration of proprioceptive and exteroceptive sensors. In *2018 IEEE international conference on robotics and automation (ICRA)*, pages 2448–2453. IEEE, 2018.

Stefano Stassi, Valentina Cauda, Giancarlo Canavese, and Candido Fabrizio Pirri. Flexible tactile sensing based on piezoresistive composites: A review. *Sensors*, 14(3):5296–5332, 2014.

Stratasys. Agilus30 material data sheet 2022, 2022a. URL `https://www.stratasysdirect.com/-/media/files/direct/material-datasheets/polyjet/pj_agilus30_material_datasheet_201802.pdf?la=en&hash=BDBDA2FF296C18D1769626151232C42E19A12343`.

Stratasys. Vero material data sheet 2022, 2022b. URL `https://www.stratasys.com/-/media/files/material-spec-sheets/mds_pj_vero_for_j55_0320a.pdf`.

Yinyin Su, Zhonggui Fang, Wenpei Zhu, Xiaochen Sun, Yuming Zhu, Hexiang Wang, Kailuan Tang, Hailin Huang, Sicong Liu, and Zheng Wang. A high-payload proprioceptive hybrid robotic gripper with soft origamic actuators. *IEEE Robotics and Automation Letters*, 5(2):3003–3010, 2020.

Javier Tapia, Espen Knoop, Mojmir Mutnỳ, Miguel A Otaduy, and Moritz Bächer. Makesense: Automated sensor design for proprioceptive soft robots. *Soft robotics*, 7(3):332–345, 2020.

Seppe Terryn, Jakob Langenbach, Ellen Roels, Joost Brancart, Camille Bakkali-Hassani, Quentin-Arthur Poutrel, Antonia Georgopoulou, Thomas George Thuruthel, Ali Safaei, Pasquale Ferrentino, et al. A review on self-healing polymers for soft robotics. *Materials Today*, 47:187–205, 2021.

Thomas George Thuruthel, Benjamin Shih, Cecilia Laschi, and Michael Thomas Tolley. Soft robot perception using embedded soft sensors and recurrent neural networks. *Science Robotics*, 4(26), 2019.

Yasunori Toshimitsu, Ki Wan Wong, Thomas Buchner, and Robert Katzschmann. Sopra: Fabrication & dynamical modeling of a scalable soft continuum robotic arm with integrated proprioceptive sensing. *arXiv preprint arXiv:2103.10726*, 2021.

Massimo Totaro, Alessio Mondini, Andrea Bellacicca, Paolo Milani, and Lucia Beccai. Integrated simultaneous detection of tactile and bending cues for soft robotics. *Soft robotics*, 4(4):400–410, 2017.

Ryan L Truby, Michael Wehner, Abigail K Grosskopf, Daniel M Vogt, Sebastien GM Uzel, Robert J Wood, and Jennifer A Lewis. Soft somatosensitive actuators via embedded 3d printing. *Advanced Materials*, 30(15):1706383, 2018.

Ryan L Truby, Cosimo Della Santina, and Daniela Rus. Distributed proprioception of 3d configuration in soft, sensorized robots via deep learning. *IEEE Robotics and Automation Letters*, 5(2):3299–3306, 2020.

IM Van Meerbeek, CM De Sa, and RF Shepherd. Soft optoelectronic sensory foams with proprioception. *Science Robotics*, 3(24), 2018.

Lucie Viry, Alessandro Levi, Massimo Totaro, Alessio Mondini, Virgilio Mattoli, Barbara Mazzolai, and Lucia Beccai. Flexible three-axial force sensor for soft and highly sensitive artificial touch. *Advanced materials*, 26(17):2659–2664, 2014.

Francesco Visentin, Giovanna A Naselli, and Barbara Mazzolai. A new exploration strategy for soft robots based on proprioception. In *2020 3rd IEEE International Conference on Soft Robotics (RoboSoft)*, pages 816–821. IEEE, 2020.

Ivan Vitanov, Ataka Rizqi, and Kaspar Althoefer. Shape reconstruction of soft-body manipulator: A learning-based approach. In *Annual Conference Towards Autonomous Robotic Systems*, pages 58–61. Springer, 2020.

Hesheng Wang, Runxi Zhang, Weidong Chen, Xinwu Liang, and Rolf Pfeifer. Shape detection algorithm for soft manipulator based on fiber bragg gratings. *IEEE/ASME Transactions on Mechatronics*, 21(6): 2977–2982, 2016a.

Hongbo Wang, Greg De Boer, Junwai Kow, Ali Alazmani, Mazdak Ghajari, Robert Hewson, and Peter Culmer. Design methodology for magnetic field-based soft tri-axis tactile sensors. *Sensors*, 16(9):1356, 2016b.

Hongbo Wang, Dominic Jones, Gregory de Boer, Junwai Kow, Lucia Beccai, Ali Alazmani, and Peter Culmer. Design and characterization of tri-axis soft inductive tactile sensors. *IEEE Sensors Journal*, 18 (19):7793–7801, 2018a.

Hongbo Wang, Junwai Kow, Nicholas Raske, Gregory De Boer, Mazdak Ghajari, Robert Hewson, Ali Alazmani, and Peter Culmer. Robust and high-performance soft inductive tactile sensors based on the eddy-current effect. *Sensors and Actuators A: Physical*, 271:44–52, 2018b.

Hongbo Wang, Massimo Totaro, and Lucia Beccai. Toward perceptive soft robots: Progress and challenges. *Advanced Science*, 5(9):1800541, 2018c.

Jue Wang and Alex Chortos. Control strategies for soft robot systems. *Advanced Intelligent Systems*, 4(5): 2100165, 2022.

Robert J Webster III and Bryan A Jones. Design and kinematic modeling of constant curvature continuum robots: A review. *The International Journal of Robotics Research*, 29(13):1661–1683, 2010.

Edward L White, Jennifer C Case, and Rebecca K Kramer. Multi-mode strain and curvature sensors for soft robotic applications. *Sensors and Actuators A: Physical*, 253:188–197, 2017.

Helge A Wurdemann, Sina Sareh, Ali Shafti, Yohan Noh, Angela Faragasso, Damith S Chathuranga, Hongbin Liu, Shinichi Hirai, and Kaspar Althoefer. Embedded electro-conductive yarn for shape sensing of soft robotic manipulators. In *2015 37th Annual International Conference of the IEEE Engineering in Medicine and Biology Society (EMBC)*, pages 8026–8029. IEEE, 2015.

Zhexin Xie, Feiyang Yuan, Zemin Liu, Zhaoning Sun, Elias M Knubben, and Li Wen. A proprioceptive soft tentacle gripper based on crosswise stretchable sensors. *IEEE/ASME Transactions on Mechatronics*, 25(4):1841–1850, 2020.

Yohta Yamamoto, Kenji Kure, Takayoshi Iwai, Takefumi Kanda, and Koichi Suzumori. Flexible displacement sensor using piezoelectric polymer for intelligent fma. In *2007 IEEE/RSJ International Conference on Intelligent Robots and Systems*, pages 765–770. IEEE, 2007.

Michelle C Yuen, Rebecca Kramer-Bottiglio, and Jamie Paik. Strain sensor-embedded soft pneumatic actuators for extension and bending feedback. In *2018 IEEE International Conference on Soft Robotics (RoboSoft)*, pages 202–207. IEEE, 2018.

Sungryul Yun, Suntak Park, Bongje Park, Youngsung Kim, Seung Koo Park, Saekwang Nam, and Ki-Uk Kyung. Polymer-waveguide-based flexible tactile sensor array for dynamic response. *Advanced materials*, 26(26):4474–4480, 2014.

Shao-Hui Zhang, Feng-Xia Wang, Jia-Jia Li, Hong-Dan Peng, Jing-Hui Yan, and Ge-Bo Pan. Wearable wide-range strain sensors based on ionic liquids and monitoring of human activities. *Sensors*, 17(11): 2621, 2017.

Huichan Zhao, Kevin O'Brien, Shuo Li, and Robert F Shepherd. Optoelectronically innervated soft prosthetic hand via stretchable optical waveguides. *Science robotics*, 1(1):eaai7529, 2016.

Qingxiang Zhao, Jiewen Lai, and Henry Chu. Reconstructing external force on the circumferential body of continuum robot with embedded proprioceptive sensors. *IEEE Transactions on Industrial Electronics*,

2021.

Wei Zhuang, Guangkai Sun, Hong Li, Xiaoping Lou, Mingli Dong, and Lianqing Zhu. Fbg based shape sensing of a silicone octopus tentacle model for soft robotics. *Optik*, 165:7–15, 2018.